

# Diamond Jet Hybrid HVOF Thermal Spray: Gas-Phase and Particle Behavior Modeling and Feedback Control Design

Mingheng Li, Dan Shi, and Panagiotis D. Christofides\*

Department of Chemical Engineering, University of California, Los Angeles, California 90095-1592

This paper focuses on the modeling and control of an industrial high-velocity oxygen-fuel (HVOF) thermal spray process (Diamond Jet hybrid gun, Sulzer Metco, Westbury, NY). We initially develop a fundamental model for the process that describes the evolution of the gas thermal and velocity fields and the motion and temperature of particles of different sizes and explicitly accounts for the effect of the powder size distribution. Using the proposed model, a comprehensive parametric analysis is performed to systematically characterize the influence of controllable process variables such as the combustion pressure and oxygen/fuel ratio, as well as the effect of the powder size distribution, on the values of the particle velocity, temperature, and degree of melting at the point of impact on the substrate. (These are the variables that directly influence coating microstructure and porosity, which, in turn, determine coating strength and hardness; see the second article of this series for details.) A feedback control system that aims to control the volume-based average particle velocity and melting ratio by directly manipulating the flow rates of fuel, oxygen, and air at the entrance of the HVOF gun is developed and applied to a detailed mathematical model of the process. Closed-loop simulations show that the feedback controller is effective in driving the controlled outputs to the desired set-point values and is also robust with respect to various kinds of disturbances in the operating environment.

## 1. Introduction

The past two decades have witnessed the wide application of high-velocity oxygen-fuel (HVOF) thermal spray technology (see Figure 1 for a schematic of this process) as a means for depositing coatings of cermets, metallic alloys, and composites to modify the surface properties of a base material (substrate). Using the thermal energy produced by the combustion of fuel with oxygen to heat and propel the powder particles, the HVOF thermal spray provides a highly efficient way to modify the surface properties of a substrate to extend product life, increase performance, and reduce maintenance costs. Recently, there has been increasing interest in the HVOF thermal spray processing of nanostructured coatings whose grain size is less than about 100 nm.<sup>1</sup> This interest has been motivated by several factors, including (1) the cost-effective production of high-quality nanosize powders; (2) the superior qualities of coatings made with the HVOF process;<sup>2</sup> and (3) the discovery that nanostructured coatings exhibit superior qualities over traditional counterparts (made of materials with micro-sized grains) in several aspects including hardness, strength, ductility, and diffusivity.<sup>1,3</sup>

Over the past decade, the need to optimally design and operate thermal spray processes has motivated significant research on the development of fundamental mathematical models to capture the various physicochemical phenomena taking place during thermal spray processes and to describe the dynamic behavior of various process components. Specifically, fundamental models have been developed describing the gas dynamics and particle in-flight behavior inside the gun and in the free jet;<sup>4–6</sup> molten droplet deposition, solidification, and microstructure development;<sup>7,8</sup> and the relationship

between coating microstructure and mechanical properties.<sup>9</sup> In addition, research has been carried out on the integration of the detailed models of the aforementioned components to develop general simulators that describe the behavior of the entire thermal spray processes.<sup>8,10</sup>

To reduce product variability and to improve robustness with respect to variations in the operating conditions in industrial HVOF thermal spray processes, it is important to implement excellent real-time process diagnosis and control that can lead to the fabrication of coatings with microstructures that yield the desired properties. Despite the recent progress on the modeling of the various phenomena that affect droplet motion, deposition, solidification, and microstructure development in HVOF thermal spray processes, no systematic framework currently exists for the integrated on-line diagnosis and control of the HVOF thermal spray process that is capable of achieving precise regulation of the microstructure and ultimate mechanical and thermal properties of the sprayed coatings. In addition, incorporation of advanced real-time diagnosis and control schemes into thermal spray processes is expected to reduce operating costs and environmental impacts and allow for the deposition of nanostructured and complex (multimaterial) coatings with very low variability. Because the application of optimization and control techniques to spray casting processes has been reported to lead to significant improvements in their operation and performance,<sup>11,12</sup> it is important to develop real-time computer control systems for thermal spray processes by integrating fundamental models that accurately describe the inherent relationships between the coating microstructure and the processing parameters with on-line state-of-the-art diagnostic techniques and control algorithms. Recent efforts in this direction have mainly focused on diagnostics and control of plasma thermal spray,<sup>13</sup> the reader can refer to Moreau

\* To whom correspondence should be addressed. Tel.: (310)-794-1015. Fax: (310)206-4107. E-mail: pdc@seas.ucla.edu.

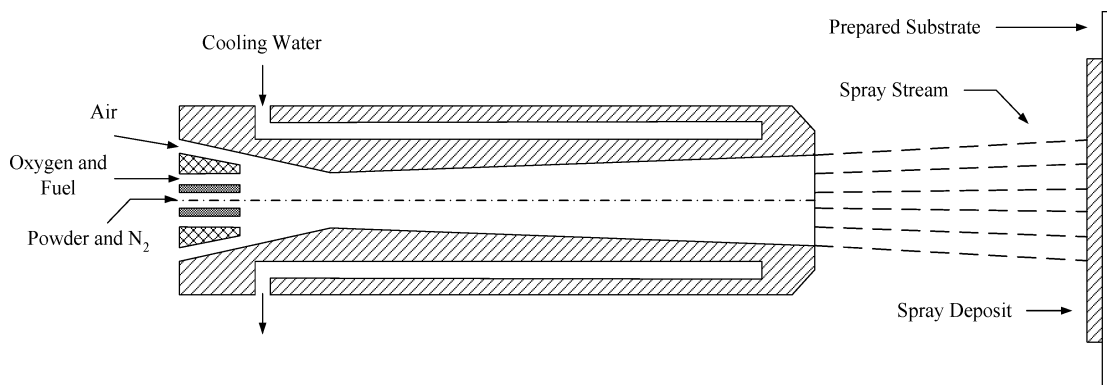


**Figure 1.** Schematic of the Diamond Jet hybrid HVOF thermal spray process.

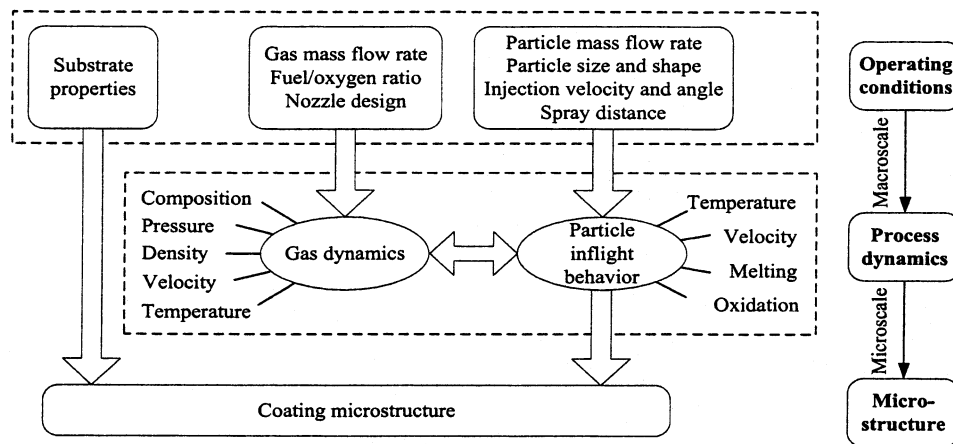


**Figure 2.** Multiscale character of the HVOF thermal spray process.

and Leblanc<sup>14</sup> for a discussion of various process optimization and control issues. In our previous work,<sup>15,16</sup> we performed a comprehensive control-relevant parametric analysis and proposed a novel formulation of the control problem that accounts for the important effect of the powder size distribution for an HVOF process in which air is used as the oxidant and propane is used as the fuel gas.

The objective of the present research is to develop a computational methodology to precisely control the coating micro- or nanostructure that determines the coating mechanical and physical properties by manipulating macroscale operating conditions such as the gas flow rate and spray distance. The major challenge on this problem lies in the development of multiscale models linking the macroscopic-scale process behavior (i.e., gas dynamics and particle in-flight behavior) and the microscopic-scale process characteristics (evolution of coating microstructure) and the integration of models, measurements, and control theory to develop measurement/model-based control strategies.<sup>17</sup> The underlying multiscale behavior of the HVOF process is shown in Figure 2. On one hand, the microstructure of thermally sprayed coatings results from the deformation, solidification, and sintering of the deposited particles, which are dependent on the substrate properties (e.g., substrate temperature), as well as the physical and chemical state (e.g., temperature, velocity, melting ratio, and oxidant content, etc.) of the particles at the point of impact on the substrate. On the other hand, the particle in-flight behavior is coupled with the gas dynamics, which can be manipulated by adjusting operating conditions such as the total gas flow rate and the fuel/oxygen ratio. Whereas the macroscopic thermal/flow field can

be readily described by continuum-type differential equations governing the compressible two-phase flow, the process of particle deposition is stochastic and discrete in nature, and thus, it can be best described by stochastic simulation methods.<sup>18</sup>

This article is the first in a series of two articles focusing on the modeling and control of an industrial high-velocity oxygen-fuel (HVOF) thermal spray process (Diamond Jet hybrid gun, Sulzer Metco, Westbury, NY). We initially develop a fundamental model for the process that describes the evolution of the gas thermal and velocity fields and the motion and temperature of agglomerate particles of different sizes and explicitly accounts for the effect of the powder size distribution. In addition to providing useful insight into the in-flight behavior of different-size particles, the model is used to perform a comprehensive parametric analysis of the HVOF process. This analysis allows us to systematically characterize the influence of controllable process variables such as the combustion pressure and oxygen/fuel ratio, as well as the effect of the powder size distribution, on the values of the particle velocity and temperature at the point of impact on the substrate. Specifically, this study shows that the particle velocity is primarily influenced by the combustion pressure and the particle temperature is strongly dependent on the fuel/oxygen ratio. These findings are consistent with existing experimental studies and set the basis for the formulation of the control problem for the HVOF thermal spray process. To develop a feedback controller that can be readily implemented in practice, the control problem is formulated as one of regulating volume-based averages of the melting ratio and velocity of the particles at the point of impact on the substrate (these are the

**Table 1. Dimensions of the Air Cap**

parameter	value
inlet diameter (mm)	14
nozzle diameter (mm)	7.16
outlet diameter (mm)	11
inlet half-angle (deg)	12
outlet half-angle (deg)	2
length of convergent part (mm)	16
length of divergent part (mm)	54

variables that directly influence coating microstructure and porosity, which, in turn, determine coating strength and hardness) by directly manipulating the flow rates of fuel, oxygen, and air at the entrance of the HVOF thermal spray gun. A feedback control system is developed and applied to a detailed mathematical model of the process. Closed-loop simulations demonstrate that the particle velocity and melting ratio at the point of impact on the substrate reach the desired set-point values in a short time, which validates the feasibility of real-time implementation of feedback control on the HVOF thermal spray system. It is also shown that the proposed control problem formulation and the feedback control system are robust with respect to disturbances in spray distance and particle injection velocity, as well as variations in the powder size distribution.

In the second article of this series,<sup>19</sup> we present a stochastic model that uses information about the particle velocity, temperature, and degree of melting at the point of impact on the substrate from the model developed in the present paper to predict coating porosity and microstructure.

## 2. Modeling of Gas Thermal and Flow Fields

**2.1. Process Description and Modeling Procedure.** Figure 1 shows a schematic diagram of the Diamond Jet hybrid gun. The premixed fuel (typically propylene or hydrogen) and oxygen are fed from the annular gap to the air cap (also referred to as a convergent-divergent nozzle, whose dimensions are shown in Table 1), where they react to produce high-temperature combustion gases. The exhaust gases, together with the air injected from the annular inlet orifice, expand through the nozzle to reach supersonic velocity. The air cap is water-cooled to prevent it from melting. The powder particles are injected from the central inlet hole using nitrogen as the carrier gas. Consequently, rapid momentum and heat transfer between the gas and the powder particles leads to acceleration and heating of the powder particles. The molten or semimolten particles exit the air cap and move toward the substrate. The particles hit the substrate, cool, and solidify, forming a thin layer of a dense and hard coating. In the remainder of this section, we present the procedure that we follow for modeling, as well as the equations describing the gas flow and thermal fields.

Roughly speaking, three major physicochemical processes are involved in the HVOF thermal spray process: transformation of chemical energy into thermal energy by the combustion of the fuel, conversion of thermal energy into kinetic energy of the burning gases by passage through the nozzle, and transfer of momentum and heat from the gases to the powder particles. These processes occur simultaneously and make the fundamental modeling of the HVOF process a very difficult task. For example, detailed fundamental mod-

eling of the gas flow and thermal fields requires state-of-the-art computational fluid dynamics (CFD) methodologies and leads to complex two- or three-dimensional time-dependent partial differential equations.<sup>6,20,21</sup> For the purposes of control system design and implementation, a compromise between model complexity, computational cost, and model ability to capture the dominant (from a control point of view) phenomena occurring in the process is essential. To simplify the analysis, the process model used in this paper is based on the one-way coupling assumption, i.e., the presence of the particles has a minimal influence on the gas dynamics, whereas the particle in-flight behavior is dependent on the gas thermal/flow field. This assumption is reasonably accurate because the particle loading in the HVOF process, which is defined as the ratio of the mass flow rate of the particles to that of gases, is typically less than 4%.<sup>5</sup> In addition, the assumptions of instantaneous equilibrium at the entrance of the HVOF gun and frozen isentropic flow during passage through the nozzle are made. These assumptions were initially proposed and justified by Swank et al.<sup>22</sup> on the basis of a comparison of numerical simulations and experimental results and later also recommended by Cheng et al.<sup>2</sup> Comparisons of simulation results and experimental data shown later in this paper further substantiate the validity of these assumptions (see discussion in subsections 4.1 and 4.2).

Regarding the role of the air stream, it is especially difficult to predict what portion of the air takes part in the reaction. Whereas the air has been treated as a coolant solely to isolate the wall from the high-temperature flame gases in some references,<sup>23,24</sup> in others,<sup>9,20,21</sup> it has been assumed that all of the oxygen coming from the air participates in the reaction. The latter assumption is employed here, as it was pointed out clearly by Gourlaouen et al.<sup>9</sup> that the airflow mixing with the oxygen/propylene mixture should be more effective in the currently used Diamond Jet hybrid gun (which is the process under consideration in this work) than the previously used Diamond Jet gun, as implied by the "water-cooled" (not "air-cooled") nozzle. Other assumptions in the model are as follows: (1) All gases obey the ideal gas law. (2) The combustion gases behave as a perfect gas during isentropic compression and expansion, and the specific heat ratio is nearly constant. (3) The effects of friction and cooling water along the nozzle and barrel are negligible, so that the laws of isentropic flow of compressible fluids apply.

Because the flow is choked at the throat of the nozzle, the convergent part of the air cap and the divergent part can be solved separately.<sup>21</sup> The modeling procedure that is followed in the simulation is based on the sequential modular method. Specifically, given the mass flow rates of each stream (fuel, oxygen, air, and carrier gas) and a postulated combustion pressure, the temperature and gas composition at the entrance of the nozzle is calculated using an instantaneous equilibrium model, and then the nozzle flow is solved using standard isentropic compressible flow relationships. The total mass flow rate at the throat of the nozzle is then calculated and compared with that at the entrance. The combustion pressure is then adjusted using the shooting method<sup>25</sup> until the discrepancy between the calculated and specified values of the total mass flow rate falls below the specified tolerance. After the gas properties at the nozzle throat are determined, the divergent part is solved using

isentropic flow relationships. The external thermal/flow field in the free jet is described by empirical formulas.

**2.2. Modeling of the Gas Thermal and Flow Fields inside the Gun.** To calculate the equilibrium composition and temperature of the combustion gases, the method of minimization of the Gibbs free energy under adiabatic conditions is employed. This approach is advantageous compared to the equilibrium constant method because it can track a large number of species simultaneously without specifying a set of reactions a priori.<sup>26</sup> Under the assumption of adiabatic combustion under constant pressure, the calculation of equilibrium temperature and composition can be formulated as an optimization problem of the following form

$$\begin{aligned} \min G &= \sum_{j \in \text{pr}} \mu_j^{\xi_j} \\ \text{s.t.} \\ 0 &= \sum_{j \in \text{pr}} a_{ij} \xi_j - b_i^0 \quad (i = 1, \dots, l) \\ &\quad \text{(mass balance)} \\ 0 &= \sum_{j \in \text{pr}} \xi_j H_j^{\circ}(T_{\text{eq}}) + \frac{1}{2} v_{\text{eq}}^2 - h_0 - E_0 \\ &\quad \text{(energy balance)} \end{aligned} \quad (1)$$

where  $G$  is the Gibbs free energy of the product mixture (including inert gases and excess reactants); pr stands for products;  $\xi_j$ ,  $H_j$ , and  $\mu_j$  correspond to the stoichiometric coefficient, enthalpy, and chemical potential of species  $i$ , respectively;  $T_{\text{eq}}$  is the equilibrium temperature (subscript eq represents equilibrium);  $a_{ij}$  is the number of elements  $i$  in species  $j$ ;  $l$  is the total number of chemical elements involved in the system; and the superscript  $\circ$  stands for standard conditions.  $b_i^0 = \sum_{k \in \text{re}} a_{ik} \xi_k$  is the number of moles of elements  $i$  per kilogram of reactants (subscript re represents reactants),  $h_0 = \sum_{k \in \text{re}} \xi_k H_k^{\circ}(T_{\text{in}})$  is the enthalpy per kilogram of reactants (subscript in represents inlet), and  $E_0 = \sum_{k \in \text{re}} \frac{1}{2} \xi_k M_k v_k^2$  is the kinetic energy per kilogram of reactants ( $M_k$  is the molecular weight and  $v_k$  is the velocity of species  $k$ ). For a gas obeying the ideal gas law, the chemical potential can be determined by the following expression

$$\mu_i(T) = \mu_i^{\circ}(T) + RT \ln \frac{P}{P^{\circ}} + RT \ln \frac{\xi_i}{\sum_{i \in \text{pr}} \xi_i} \quad (2)$$

where  $R$  is the gas constant and  $P$  is the pressure. By continuity, the gas velocity after the combustion reaction is given by

$$v_{\text{eq}} = \frac{\dot{m}_g}{\rho A_{\text{in}}} = \frac{\dot{m}_g R T_{\text{eq}}}{P A_{\text{in}} \bar{M}_{\text{pr}}} = \frac{\dot{m}_g \xi_T R T_{\text{eq}}}{P A_{\text{in}}} \quad (3)$$

where  $\dot{m}_g$  is the total mass flow rate of the gas,  $A_{\text{in}}$  is the cross-sectional area at the inlet of the air cap,  $\bar{M}_{\text{pr}}$  is the average molecular weight of the product mixture, and  $\xi_T = \sum_{j \in \text{pr}} \xi_j$ . From eq 3, it follows that

$$\frac{1}{2} v_{\text{eq}}^2 = \frac{\dot{m}_g^2 \xi_T^2 R^2 T_{\text{eq}}^2}{2 P^2 A_{\text{in}}^2} \quad (4)$$

Defining  $f = G + \sum_{i=1}^l \lambda_i (\sum_{j \in \text{pr}} a_{ij} \xi_j - b_i^0)$ , where  $\lambda_i$  represents the so-called Lagrangian multipliers, the optimal solution of the optimization problem of eq 1 can be determined by solving the following nonlinear algebraic equations

$$\begin{aligned} 0 &= \mu_j^{\circ} + RT_{\text{eq}} \ln(P/P^{\circ}) + RT_{\text{eq}} \ln(\xi_j/\xi_T) + \sum_{i \in l} \lambda_i a_{ij} \quad (j = 1, \dots, s) \\ 0 &= \sum_{j \in \text{pr}} a_{ij} \xi_j - b_i^0 \quad (i = 1, \dots, l) \\ 0 &= \sum_{j \in \text{pr}} \xi_j - \xi_T \\ 0 &= \sum_{j \in \text{pr}} \xi_j H_j^{\circ}(T_{\text{eq}}) + \frac{\dot{m}_g^2 \xi_T^2 R^2 T_{\text{eq}}^2}{2 P^2 A_{\text{in}}^2} - h_0 - E_0 \end{aligned} \quad (5)$$

The variables to be determined are the equilibrium compositions  $\xi_j$  ( $j = 1, \dots, s$ ), the Lagrangian multipliers  $\lambda_i$  ( $i = 1, \dots, l$ ), the total number of moles  $\xi_T$ , and the equilibrium temperature  $T_{\text{eq}}$ . The set of  $s + l + 2$  nonlinear algebraic equations of problem 5 are solved using the descent Newton–Raphson method. The central idea of the Newton–Raphson method is to apply multivariable Taylor series expansion to a nonlinear vector function, truncate all terms that contain derivatives of second order and higher, and then use the resulting expression to build an iterative formula that can be used to compute the solution given an initial guess that is close to the solution; the reader is directed to ref 25 for details.

Because  $\xi_j$ ,  $\xi_T$ , and  $T$  should be positive numbers, to avoid taking the logarithm of negative numbers in the iteration procedure, we have chosen  $\Delta \ln \xi_j$  ( $j = 1, \dots, s$ ),  $\Delta \ln \xi_T$ ,  $\Delta \ln T$ , and  $-\lambda_i/RT$  ( $i = 1, \dots, l$ ) as the solution variables at each iteration step. In the above equations, the thermodynamic data, such as the heat capacity, enthalpy, entropy, and chemical potential of each species, are calculated by the following equations<sup>26</sup>

$$\begin{aligned} \frac{C_p^{\circ}(T)}{R} &= \frac{a_1}{T^2} + \frac{a_2}{T} + a_3 + a_4 T + a_5 T^2 + a_6 T^3 + a_7 T^4 \\ \frac{H^{\circ}(T)}{RT} &= -\frac{a_1}{T^2} + \frac{a_2}{T} \ln T + a_3 + \frac{a_4}{2} T + \frac{a_5}{3} T^2 + \frac{a_6}{4} T^3 + \frac{a_7}{5} T^4 + \frac{a_8}{T} \end{aligned} \quad (6)$$

$$\frac{S^{\circ}(T)}{R} = -\frac{a_1}{2T^2} - \frac{a_2}{T} + a_3 \ln T + a_4 T + \frac{a_5}{2} T^2 + \frac{a_6}{3} T^3 + \frac{a_7}{4} T^4 + a_9$$

$$\frac{\mu_j^{\circ}}{RT} = \frac{H^{\circ}(T)}{RT} - \frac{S^{\circ}(T)}{R}$$

where  $a_1$ – $a_9$  are constants for a given species. About 10 iterations are usually required to obtain a convergent solution.

Under the assumption of isentropic frozen flow, the properties of the gas phase during passage through the

nozzle (both the convergent part and the divergent part) can be solved using the following equations (which are derived by solving the conservation equations governing compressible flow)<sup>27</sup>

$$\frac{A_2}{A_1} = \frac{\mathcal{M}_1 \left\{ 1 + [(\gamma - 1)/2] \mathcal{M}_2^2 \right\}^{(\gamma+1)/2(\gamma-1)}}{\mathcal{M}_2 \left\{ 1 + [(\gamma - 1)/2] \mathcal{M}_1^2 \right\}} \quad (7)$$

$$\frac{T_2}{T_1} = \frac{1 + [(\gamma - 1)/2] \mathcal{M}_1^2}{1 + [(\gamma - 1)/2] \mathcal{M}_2^2} \quad (8)$$

$$\frac{P_2}{P_1} = \left\{ \frac{1 + [(\gamma - 1)/2] \mathcal{M}_1^2}{1 + [(\gamma - 1)/2] \mathcal{M}_2^2} \right\}^{\gamma/(\gamma-1)} \quad (9)$$

$$\frac{\rho_2}{\rho_1} = \left\{ \frac{1 + [(\gamma - 1)/2] \mathcal{M}_1^2}{1 + [(\gamma - 1)/2] \mathcal{M}_2^2} \right\}^{1/(\gamma-1)} \quad (10)$$

where  $A$  is the cross-sectional area perpendicular to the flow direction,  $\rho$  is the gas density,  $\gamma$  is the specific heat ratio calculated by the expression  $\gamma = \bar{c}_p / (\bar{c}_p - R)$  where  $\bar{c}_p = \sum_i \xi_i c_{p,i} / \sum_i \xi_i$ , and  $\mathcal{M}$  is the mach number defined by the ratio of the gas velocity to the local sonic velocity ( $a = \sqrt{\gamma P / \rho}$ ). At the throat of the nozzle, where the mach number is 1,<sup>27</sup> the mass flow rate can be calculated using the formula

$$\dot{m}_g = \rho_t v_t A_t = \sqrt{\gamma P_t \rho_t} A_t \quad (11)$$

where the subscript g stands for gas and the subscript t stands for throat. With a postulated combustion pressure, the calculated mass flow rate at the throat is usually different from that at the entrance of the gun. The shooting method is then applied to adjust the combustion pressure until these two flow rates match.

We note that the isentropic relationships (eqs 7–10) are valid only if there is no shock inside of the nozzle. This can be guaranteed as long as the following inequality holds

$$\frac{P_b}{P_e} < \frac{2\gamma}{\gamma + 1} \mathcal{M}_e^2 - \frac{\gamma - 1}{\gamma + 1} \quad (12)$$

where  $P_b$  is the back-pressure (ambient pressure) and  $P_e$  is the gas pressure at the exit of the nozzle. For the experimental Diamond Jet hybrid gun system, our calculations show that the right-hand side of the above equation is about 5, and therefore no shock will ever occur inside of the nozzle as long as the exit pressure is larger than one-fifth of the back-pressure, a condition that is always satisfied under industrial operating conditions.

We have applied the above modeling procedure and equations to analyze the Diamond Jet HVOF process,<sup>21</sup> which is similar to the one shown in Figure 1 but whose nozzle has only a convergent part. The combustion products considered in our numerical simulation are Ar, CO, CO<sub>2</sub>, H, H<sub>2</sub>, H<sub>2</sub>O, NO, N<sub>2</sub>, O, O<sub>2</sub>, OH, etc. It is worth pointing out that C<sub>3</sub>H<sub>6</sub> is not one of the products under normal operating conditions. For the given four different operating conditions, the combustion pressures predicted by the above procedure are all within 6% of the experimentally measured values (see Table 2); this result is more accurate than the one obtained with the

**Table 2. Comparison of Computational and Experimental Results for a Diamond Jet Process<sup>21</sup>**

case	O <sub>2</sub> (scfh)	C <sub>3</sub> H <sub>6</sub> (scfh)	air (scfh)	N <sub>2</sub> (scfh)	P <sub>eq</sub> <sup>c</sup> (psia)	P <sub>eq</sub> <sup>f</sup> (psia)	error (%)
1	635	185	790	29.4	69.7	68.7	-1.4
2	635	185	395	29.4	59.7	56.1	-6.0
3	879	185	795	29.4	76.7	77.6	1.2
4	347	110	632	29.4	44.7	44.8	0.2

two-step chemical kinetics model<sup>21</sup> and implies that the combustion model should take into account the dissociation of the combustion products.

**2.3. Modeling of the Gas Thermal and Flow Fields outside the Gun.** At the exit of the nozzle, the Reynolds number based on the diameter and the gas velocity is about  $3 \times 10^4$ , and the flow is fully turbulent. Depending on the magnitudes of the gas pressure at the exit of the air cap and the back-pressure, the flow outside the nozzle might be underexpanded, ideally expanded, or overexpanded. Usually, the velocity and temperature of the gas in the free jet are lower than those at the nozzle exit.<sup>28,29</sup> From the exit of the nozzle to a position whose distance is not larger than the potential core length ( $L_{pc}$ ), the gas velocity and temperature can be considered almost constant.<sup>30</sup> Further downstream, the gas velocity and temperature decay rapidly because of the entrainment of the surrounding air. This decay of the gas velocity and temperature can be described by the empirical formulas<sup>30</sup>

$$\frac{v}{v_e} = 1 - \exp\left(\frac{\alpha}{1 - x/L_{pc}}\right) \quad (13)$$

and

$$\frac{T - T_a}{T_e - T_a} = 1 - \exp\left(\frac{\beta}{1 - x/L_{pc}}\right) \quad (14)$$

where  $x$  is the axial distance from the exit of the gun barrel ( $x > L_{pc}$ ) and  $\alpha$  and  $\beta$  are parameters obtained from experimental measurements.  $L_{pc}$  is a function of the mach number at the exit of the gun barrel ( $\mathcal{M}_e$ ) and the barrel diameter ( $D$ ) according to<sup>30</sup>

$$L_{pc}/D = 3.5 + 1.0 \mathcal{M}_e^2 \quad (15)$$

### 3. Modeling of Particle Motion and Temperature

The particle trajectories and temperature histories in the gas field are computed by the momentum- and heat-transfer equations. Because the acceleration and deceleration of the particles in the moving gas in the HVOF process are dominated by the drag force,<sup>31</sup> other forces applied on the particles can be neglected, and the particle motion can be adequately described by the following two first-order ordinary differential equations

$$m_p \frac{dv_p}{dt} = \frac{1}{2} C_D \rho_g A_p (v_g - v_p) |v_g - v_p|, \quad v_p(0) = v_{p0}$$

$$\frac{dx_p}{dt} = v_p, \quad x_p(0) = 0 \quad (16)$$

where  $m_p$  is the mass of the particle,  $v_p$  is the axial velocity of the particle,  $A_p$  is the projected area of the particle on the plane perpendicular to the flow direction,  $\rho_g$  is the density of the gas,  $C_D$  is the drag coefficient,

and  $x_p$  is the position of the particle. The absolute sign in the relative velocity between the particle and the gas implies that a particle is accelerated if its velocity is less than that of the gas and decelerated otherwise. To take into consideration the fact that many powders used in the HVOF process are not spherical, a formula for the drag coefficient  $C_D$  that accounts for the particle shape using the concept of sphericity  $\phi$  (defined as the ratio of the surface area of a sphere with equivalent volume to the actual surface area of the particle) is used in this paper; it has the following form<sup>32,33</sup>

$$\frac{C_D}{K_2} = \frac{24}{ReK_1K_2} [1 + 0.1118(ReK_1K_2)^{0.6567}] + \frac{0.4305}{1 + 3305/ReK_1K_2} \quad (17)$$

where  $K_1$  and  $K_2$  are two sphericity-related factors. The local Reynolds number ( $Re$ ) for this two-phase flow problem is defined on the basis of the relative velocity  $Re = d_p |v_g - v_p| \rho_g / \bar{\eta}_g$ , where  $d_p$  is either the particle diameter if the particle is spherical or an appropriate equivalent diameter if the particle is not spherical and  $\bar{\eta}_g$  is the gas viscosity.

In the HVOF process, the Biot number of the particles ( $Bi = hL/\lambda_p$ , where  $h$  is the heat-transfer coefficient,  $L$  is a characteristic dimension defined by the ratio of the particle volume to its surface area, and  $\lambda_p$  is the thermal conductivity of the particle) is typically less than 0.1,<sup>32</sup> which means that the particles are heated with negligible internal resistance and that the temperature gradients inside the particles can be neglected.<sup>34</sup> Consequently, the equation describing the heat transfer between a single particle and the gas reduces to a first-order ordinary differential equation. Depending on the value of the particle temperature, different equations are used. With the assumption of negligible particle vaporization, the particle heating can be described by

$$hA'_p(T_g - T_p) = \begin{cases} m_p c_p \frac{dT_p}{dt}, & T_p \neq T_m \\ \Delta H_m m_p \frac{df_p}{dt}, & T_p = T_m \end{cases} \quad (18)$$

where  $T_p$  is the temperature of the particle;  $A'_p$  is the surface area of the particle;  $T_m$  is the melting point of the particle;  $\Delta H_m$  is the enthalpy of melting; and  $f_p$  is the melting ratio, or the ratio of the melted mass to the total mass of the particle ( $0 \leq f_p \leq 1$ ). The heat-transfer coefficient  $h$  is computed by the Ranz–Marshall empirical equation<sup>35</sup>

$$\frac{hd_p}{\bar{\lambda}_g} = Nu = 2 + 0.6Re^{1/2} Pr^{1/3} \quad (19)$$

where the Prandtl number ( $Pr$ ) is calculated according to  $Pr = \bar{c}_p \bar{\eta}_g / \bar{\lambda}_g$ .

In the above equations, the viscosity and thermal conductivity of each species are calculated by the following formulas<sup>26</sup>

$$\begin{aligned} \ln(\eta) &= b_1 \ln(T) + b_2/T + b_3/T^2 + b_4 \\ \ln(\lambda) &= c_1 \ln(T) + c_2/T + c_3/T^2 + c_4 \end{aligned} \quad (20)$$

where  $b_1$ – $b_4$  and  $c_1$ – $c_4$  are constants for a specific species. For gas mixtures, the average viscosity and thermal conductivity are calculated by the following mixing rules<sup>26</sup>

$$\begin{aligned} \bar{\eta} &= \sum_i \frac{x_i \eta_i}{x_i + \sum_{j \neq i} x_j \psi_{ij}} \\ \bar{\lambda} &= \sum_i \frac{x_i \lambda_i}{x_i + \sum_{j \neq i} x_j \zeta_{ij}} \end{aligned} \quad (21)$$

where the interaction coefficients  $\psi_{ij}$  and  $\zeta_{ij}$  are obtained from the following formulas

$$\begin{aligned} \psi_{ij} &= \frac{1}{4} \left[ 1 + \left( \frac{\eta_i}{\eta_j} \right)^{1/2} \left( \frac{M_j}{M_i} \right)^{1/4} \right]^2 \left[ \frac{2M_j}{M_i + M_j} \right]^{1/2} \\ \zeta_{ij} &= \psi_{ij} \left[ 1 + \frac{2.41(M_i - M_j)(M_i - 0.142M_j)}{(M_i + M_j)^2} \right] \end{aligned} \quad (22)$$

At each step, we integrate eqs 16 and 18 with a small enough time step such that the gas velocity, gas temperature, and local Reynolds number can all be considered constant over this interval. After one integration step, we update the gas velocity and gas temperature according to the new particle position and then apply the same strategy for the next time step. This methodology was proposed by Crowe and Stock<sup>36</sup> and was found to be computationally economical and accurate. To account for the particle melting behavior, we modified this approach to check the molten state of the particle at each time step and apply different formulas for the particle heating. Specifically, the iterative formulas for particle velocity, position, and temperature are

$$\begin{aligned} v_p^{i+1} &= v_g^i - (v_g^i - v_p^i) \exp(-\Delta t/\tau_p) \\ x_p^{i+1} &= x_p^i + v_p^i \Delta t \\ T_p^{i+1} &= T_g^i - (T_g^i - T_p^i) \exp(-\Delta t/\omega_p), \\ &T_p^i, T_p^{i+1} > T_m \text{ or } T_p^i, T_p^{i+1} < T_m \\ f_p^{i+1} &= f_p^i + \frac{c_p(T_g^i - T_m)}{\Delta H_m} \frac{\Delta t}{\omega_p}, \quad 0 < f_p^i, f_p^{i+1} < 1 \end{aligned} \quad (23)$$

where  $\tau_p = 4\rho_p d_p^2 / 3\bar{\eta}_g C_D Re$  and  $\omega_p = \rho_p c_p d_p^2 / 6Nu\bar{\lambda}_g$ . In the four possible phase transition points, in which the current step and the next step correspond to different particle molten states, the successive formulas for particle temperature and melting ratio take the following forms:

1.  $T_p^i < T_m$  ( $f_p^i = 0$ ),  $T_p^{i+1} > T_m$ , from totally solid state to partially melted state

$$\begin{aligned} f_p^{i+1} &= f_p^i + \frac{c_p(T_p^{i+1} - T_m)}{\Delta H_m} \\ T_p^{i+1} &= T_m \end{aligned} \quad (24)$$

2.  $T_p^i > T_m$  ( $f_p^i = 1$ ),  $T_p^{i+1} < T_m$ , from totally liquid state to partially melted state

$$f_p^{i+1} = f_p^i + \frac{c_{p,p}(T_p^{i+1} - T_m)}{\Delta H_m}$$

$$T_p^{i+1} = T_m \quad (25)$$

3.  $T_p^i = T_m$  ( $0 < f_p^i < 1$ ),  $T_p^{i+1} > T_m$ , from partially melted state to totally liquid state

$$T_p^{i+1} = T_m + \frac{\Delta H_m(f_p^{i+1} - 1)}{c_{p,p}}$$

$$f_p^{i+1} = 1 \quad (26)$$

4.  $T_p^i = T_m$  ( $0 < f_p^i < 1$ ),  $T_p^{i+1} < T_m$ , from partially melted state to totally solid state

$$T_p^{i+1} = T_m + \frac{\Delta H_m f_p^{i+1}}{c_{p,p}}$$

$$f_p^{i+1} = 0 \quad (27)$$

To reduce the computation time and to maintain accuracy at the same time, a time-varying time step of the form

$$\Delta t = \min\{\tau_p/100, \omega_p/100, \Delta x_{\max}/v_p\} \quad (28)$$

is used, where  $\Delta x_{\max}$  is chosen to be  $10^{-4}$  m, which is the maximum flight distance in each time interval. The first two constraints guarantee that the gas velocity and temperature will change little in each time step.

#### 4. Analysis of Gas and Particle Behavior

**4.1. Analysis of the Gas Dynamics without Air.** Initially, we included only propylene and oxygen as the feed to the system and tested the influence of the combustion pressure and oxygen/fuel ratio on the gas temperature, velocity, density, and momentum flux ( $\rho u^2$ ) in the internal field. The reasons for this approach are the following: (1) The influence of the process parameters on the gas dynamics and the particle in-flight behavior is apparent in this simplified case. (2) A bijection of the pressure and equivalence ratio to the fuel and oxygen flow rates is possible, and calculation starting from either side is equivalent, which facilitates the numerical calculation. (3) There are many HVOF processes whose feed consists of only fuel and oxygen (i.e., without air); see, for example, Gu et al.<sup>37</sup> and Yang and Eidelman.<sup>5</sup> The process model was based on the assumptions of negligible injection gas velocity, instantaneous equilibrium under constant enthalpy and pressure in the injection interface, and frozen isentropic flow during passage through the nozzle. To account for the dissociation of gaseous products, the model included eight species (CO, CO<sub>2</sub>, H, H<sub>2</sub>, H<sub>2</sub>O, O, O<sub>2</sub>, and OH) in the product mixture. The equilibrium temperature and composition of combustion were solved by minimizing the total Gibbs free energy, and the gas properties during passage through the nozzle were determined by the standard laws governing compressible flows described in subsection 2.2.

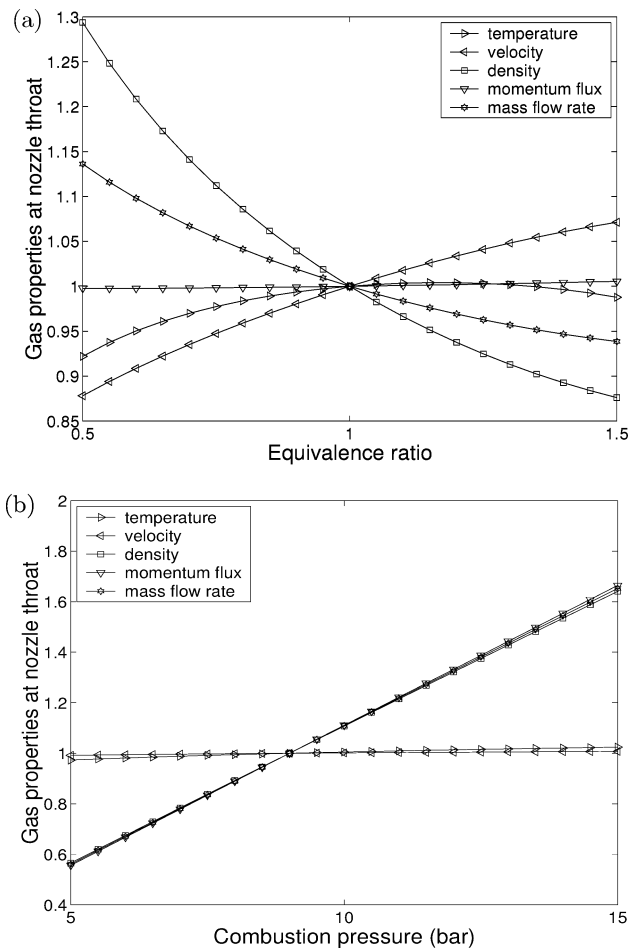


**Figure 3.** Normalized gas temperature, velocity, momentum flux, and mass flow rate in the internal field under the following operating conditions:  $P = 5\text{--}15$  bar and  $\varphi = 0.5\text{--}1.6$ . Normalization is done with respect to the corresponding gas properties under the following operating conditions:  $P = 9$  bar and  $\varphi = 1.0$  (Table 3).

**Table 3. Gas Properties under the Operating Conditions  $P = 9$  bar and  $\varphi = 1.0$**

properties	inlet	throat	exit
temperature (K)	3486.7	3120.7	2222.6
velocity (m/s)	—	1147.0	2150.8
density (kg/m <sup>3</sup> )	0.7535	0.4688	0.1073
momentum flux (10 <sup>5</sup> kg·m/s <sup>2</sup> )	—	6.1673	4.9627
mass flow rate (10 <sup>-3</sup> kg/s)	21.65	21.65	21.65
average molecular weight (10 <sup>-3</sup> kg/mol)	24.15	24.15	24.15

In Figure 3a, the combustion pressure is fixed to be 9 bar, and the equivalence ratio varies from 0.5 to 1.6. In this range, a peak is observed in each of the temperature vs equivalence ratio plots. As the equivalence ratio increases, the temperatures at the entrance, the throat, and the exit first increase, reaching a maximum value, and then decrease. However, the equivalence ratio associated with each peak temperature is about 1.2 (indicating a fuel-rich system), which is somewhat different from the value expected for a fuel/air system,<sup>15</sup> whose optimal value is close to 1.05. It can also be seen that as the equivalence ratio increases from 0.5 to 1.6, the gas velocities both at the throat and at the exit increase by about 22–23%, while the gas density decreases by about 33%. As a result, the momentum flux remains almost constant at these two positions. In Figure 3b, the equivalence ratio is kept at

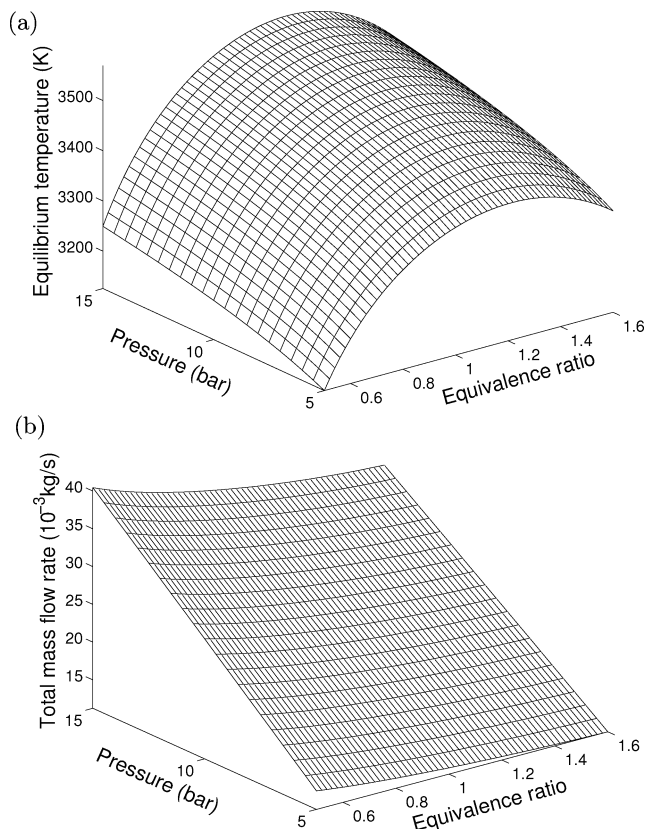


**Figure 4.** Profile of equilibrium temperature and total mass flow rate with respect to  $P$  and  $\varphi$ . Operating conditions:  $P = 5$ –15 bar and  $\varphi = 0.5$ –1.6.

1.0, and the combustion pressure varies from 5 to 15 bar. In the combustion pressure range of interest, it is found that both gas velocity and gas temperature change little (about 2 and 5%, respectively); however, the gas density and momentum flux change almost linearly with respect to the combustion pressure, by about 190 and 200%, respectively. We also computed 3D profiles of gas properties under different combustion pressures and equivalence ratios, as shown in Figures 4–6. Further analysis reveals the following:

1. At a fixed pressure, there is a peak in the equilibrium temperature vs equivalence ratio plot, whose value is about 1.2. It is worth noting that the peak flame temperature occurs not at stoichiometric, but rather at fuel-rich conditions. This is because the equilibrium temperature is determined not only by the heat generated by the exothermic reaction process, but also by the heat capacity of the product mixture. As the equivalence ratio increases to slightly above 1, the gas temperature increases further with the equivalence ratio; this is because the heat capacity of the products decreases more rapidly than the heat released. Beyond the equivalence ratio associated with the peak temperature (about 1.2), the heat generated falls more rapidly than does the heat capacity, and the temperature decreases. On the other hand, when the equivalence ratio is fixed, the equilibrium temperature increases with pressure. The primary cause of the equilibrium temperature variation with pressure is the product dissociation because higher pressure favors larger molecules (Le Chatelier's principle). Further increasing the pressure results in an increase in  $\text{H}_2\text{O}$  with respect to  $\text{H}_2$  and  $\text{O}$  and helps to increase the temperature.

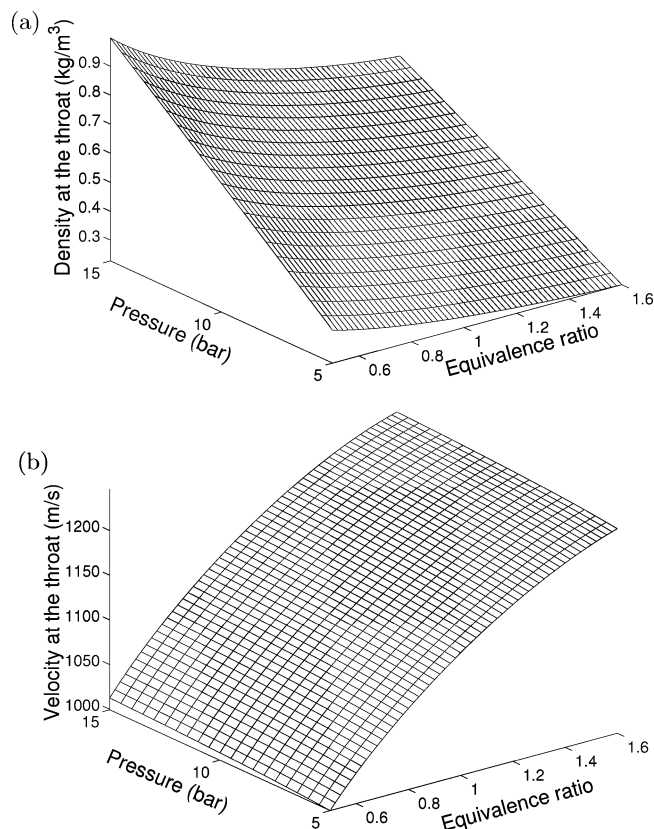


**Figure 5.** Profile of gas density and velocity at the throat with respect to  $P$  and  $\varphi$ . Operating conditions:  $P = 5$ –15 bar and  $\varphi = 0.5$ –1.6.

2. The higher the equivalence ratio, the smaller the total mass flow rate is needed to achieve the same combustion pressure to choke the flow. On the other hand, under the same equivalence ratio, the combustion pressure increases linearly with the total mass flow rate. These observations can be explained by the following equation

$$\dot{m}_g = \rho_g v_g A = \mathcal{M} P \sqrt{\frac{\gamma \bar{M}_{pr}}{RT_g}} A = \frac{\mathcal{M} P \gamma A}{a} \quad (29)$$

Note that the combustion process tends to increase the total number of moles in the product mixture and to decrease the average molecular weight. In the fuel-rich case, the total amount of dissociation becomes significant, and the molecular weight decreases continuously as  $\varphi$  increases. Referring to Figure 7, when  $\varphi$  increases from 0.5 to 1.6 for a fixed  $P$  and a <10% variation in  $T$ ,  $\bar{M}_{pr}$  decreases by about 30% following a nearly linear function, and as a consequence,  $\bar{M}_{pr}/T$  decreases monotonically. Therefore,  $\dot{m}_g$  decreases monotonically as  $\varphi$  increases. When the combustion pressure increases with a fixed  $\varphi$ , both  $\bar{M}_{pr}$  and  $T$  increase slightly because the product dissociation is suppressed. Because  $\sqrt{\bar{M}_{pr}/T}$  varies by less than 2% in the pressure range of interest, the total mass flow rate of the gas is roughly proportional to the combustion pressure. Equation 29 also indicates that the pressure can be increased by (1) increasing the total mass flow rate of the gas and (2) increasing the equivalence ratio.

3. The gas density at the nozzle throat can increase by increasing the combustion pressure and decreasing

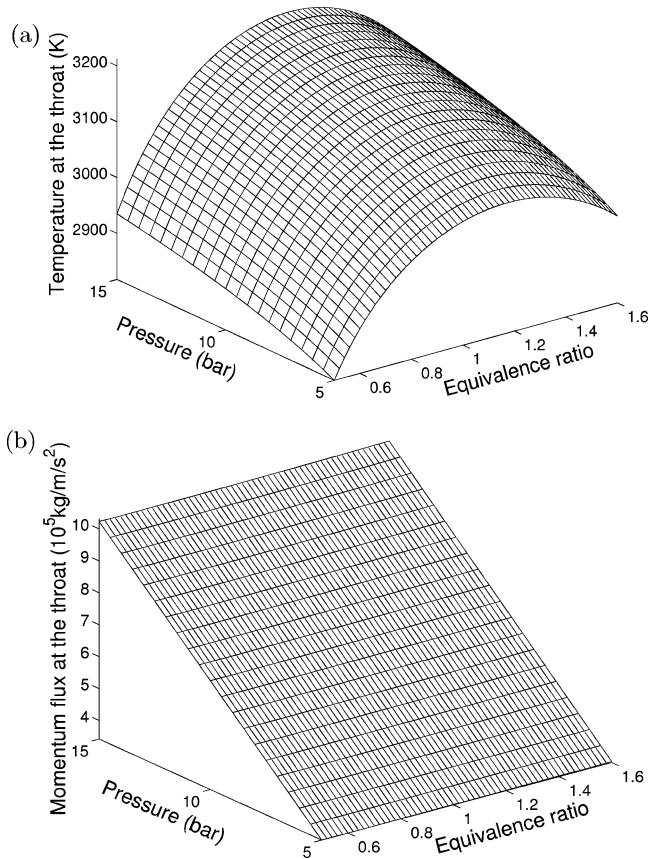


**Figure 6.** Profile of temperature and momentum flux at the throat with respect to  $P$  and  $\varphi$ . Operating conditions:  $P = 5\text{--}15$  bar and  $\varphi = 0.5\text{--}1.6$ .

the equivalence ratio. This can be explained by the expression  $\rho = \gamma P/a^2$ . However, the gas velocity at the nozzle throat, where the Mach number is one, is mainly a function of the equivalence ratio and changes little with the combustion pressure, as previously discussed.

4. The momentum flux at the throat of the nozzle is independent of the equivalence ratio and is a linear function of the combustion pressure. The influence of pressure on momentum flux can be explained by the equation

$$\rho_g v_g^2 = \rho_g \mathcal{M}^2 a^2 = \rho_g \mathcal{M}^2 (\sqrt{\gamma P / \rho_g})^2 = \mathcal{M}^2 \gamma P \quad (30)$$

where  $\gamma$  is nearly constant and  $\mathcal{M}$  mainly depends on the geometrical configuration of the nozzle. As a consequence, the momentum flux is a nearly linear function of the gas pressure. Equation 30 is also applicable to HVOF systems that include air in the feed stream.

Because the drag force, which is the dominant force determining the motion of the particles in the gas field, is approximately proportional to the gas momentum flux, and because the difference between the gas temperature and the particle temperature provides the driving force for particle heating, it follows from the above analysis that the particle temperature and velocity can be nearly independently adjusted by manipulating the equivalence ratio and the combustion pressure, respectively.

**4.2. Analysis of the Gas Dynamics Including the Air Stream.** Motivated by the conclusions drawn from the above parametric analysis, we included air in the feed stream to the HVOF process; this makes the process analysis more difficult. Assuming the air to be

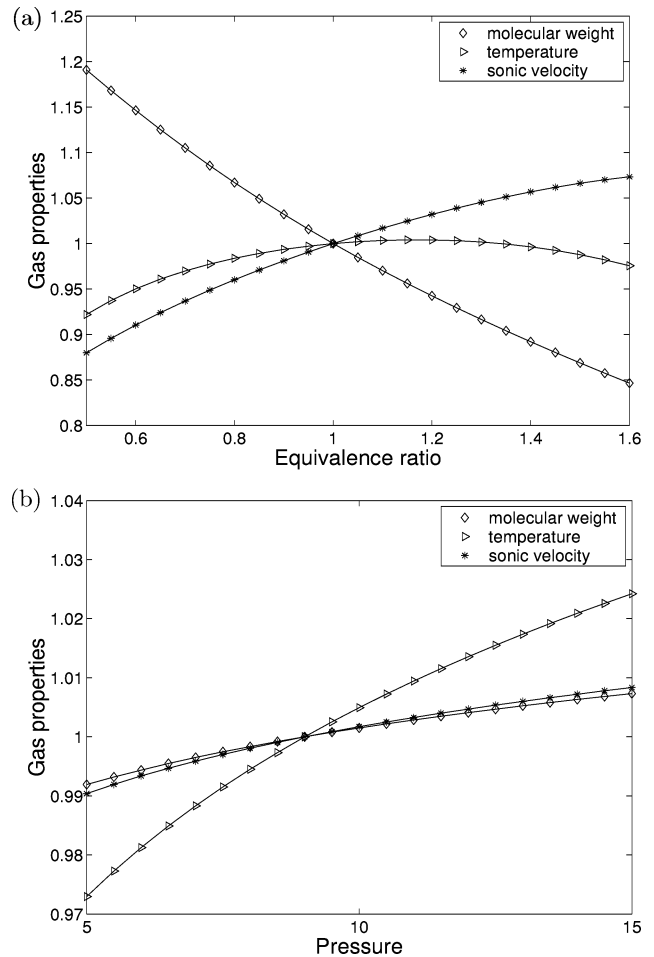
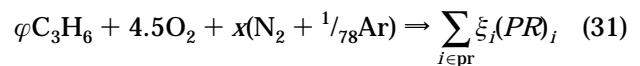


**Figure 7.** Normalized average molecular weight, temperature, and sonic velocity at the throat of the nozzle under the following operating conditions:  $P = 5\text{--}15$  bar and  $\varphi = 0.5\text{--}1.6$ . Normalization is done with respect to the corresponding gas properties under the following operating conditions:  $P = 9$  bar and  $\varphi = 1.0$  (Table 3).

composed of only  $\text{O}_2$ ,  $\text{N}_2$ , and Ar, the reaction formula becomes



where  $x$  can be any number from 0 to 16.7, corresponding to the cases of pure oxygen as the oxidant and pure air as the oxidant, respectively. Obviously, in this case, the equilibrium temperature is dependent not only on  $\varphi$ , but also on  $x$ . Furthermore, because the pressure depends on the temperature, the average molecular weight, and the mass flow rate (eq 29), the air stream plays an important role in achieving a high pressure.

Figure 8 shows the combustion pressure and equilibrium temperature under different total mass flow rates and equivalence ratios for a fixed value of  $x = 3.97$ . It can be seen that the process behavior is very similar to that observed without air if  $x$  is kept constant (compare Figures 8 and 4). The pressure contour in Figure 8a shows that the total mass flow rate required to achieve the same combustion pressure decreases as the equivalence ratio increases. The total mass flow rate increases linearly with pressure when the equivalence ratio is fixed. The equilibrium temperature is significantly dependent on the equivalence ratio, but varies only slightly with the total mass flow rate. This also implies

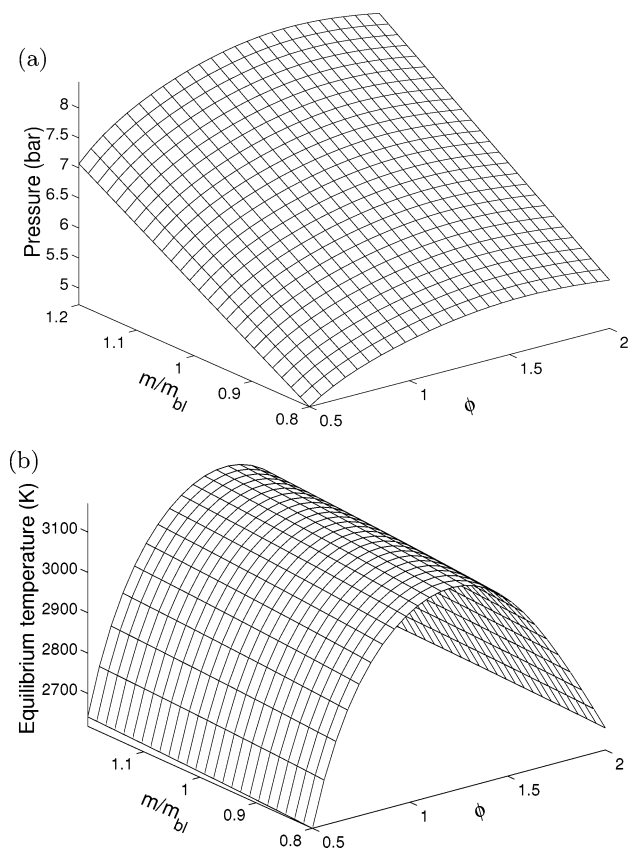


**Figure 8.** Profile of pressure and equilibrium temperature with respect to  $\phi$  and  $m/m_{bl}$ . Operating conditions:  $x$  the same as for baseline conditions [propylene, 176 scfh (standard cubic feet per hour); oxygen, 578 scfh; air, 857 scfh; nitrogen, 28.5 scfh], total mass flow rate varying from 0.8 to 1.2 times the baseline value (18.1 g/s), and  $\phi = 0.5$ –2.0.

that pressure variations do not significantly affect the equilibrium temperature.

Figure 9 shows the combustion pressure and equilibrium temperature under different equivalence ratios and oxygen/nitrogen ratios for a fixed total mass flow rate to that used under the baseline conditions. It can be seen that, as the fraction of air in the total reactant mixture increases, both the pressure and temperature drop. As  $x$  varies from 0 (pure oxygen as the oxidant) to 16.7 (pure air as the oxidant), the equivalence ratio corresponding to the peak equilibrium temperature decreases from 1.23 to 1.05 (see Figure 10); this result provides a way to optimally manipulate the relative flow rate of oxygen to air.

We tested the gas dynamics under the nine different operating conditions listed in Table 4. The baseline conditions are recommended by the manufacturer. The simulation results are reported in Table 5. Under the baseline conditions, the pressure at the exit of the air cap calculated by the proposed procedure is 0.63 bar, which implies that the flow outside the gun is overexpanded. The manufacturer, Sulzer Metco, measured a gauge pressure of  $-4$  psig ( $-0.3$  bar, or the absolute pressure is about 0.7 bar) at the nozzle exit under the same operating conditions,<sup>38</sup> which validated the model and assumptions applied in this work. In fact, the overexpanded flow condition gives a slightly higher gas velocity.

In the nine different operating conditions, the equilibrium temperature is a function of the total mass flow rate, as well as  $\phi$  and  $x$ . For instance, cases 1 and 6–9

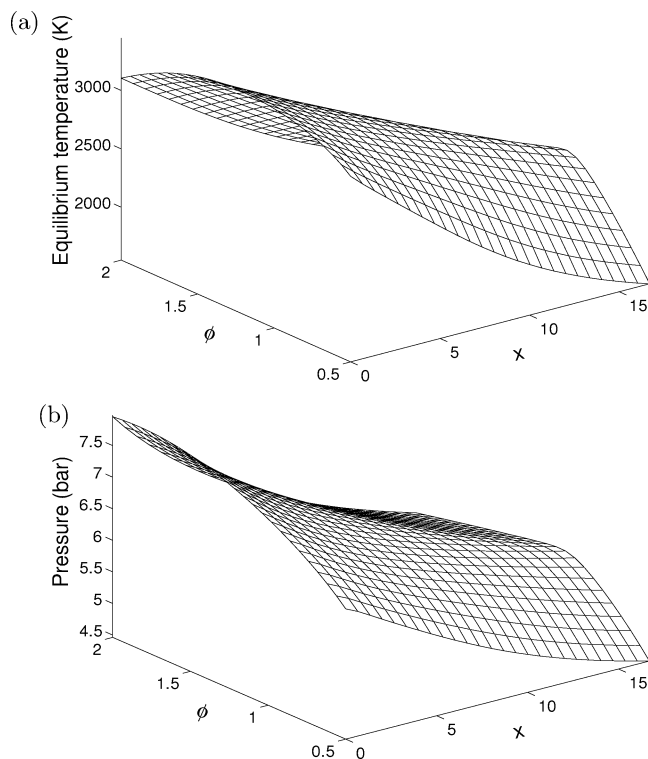


**Figure 9.** Profile of equilibrium temperature and pressure with respect to  $\phi$  and  $x$ . Operating conditions: total mass flow rate the same as for baseline conditions,  $\phi = 0.5$ –2.0, and  $x = 0$ –16.7.

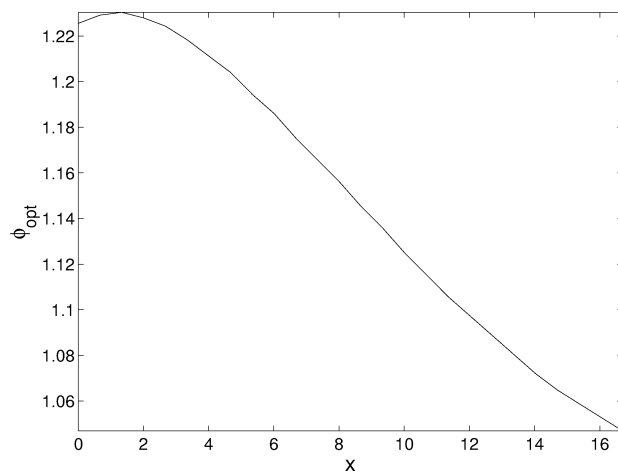


**Figure 10.** Profile of the optimal equivalence ratio corresponding to the peak temperature of the gas with respect to  $x$ . Operating conditions: total mass flow rate the same as for baseline conditions,  $x = 0$ –16.7.

**Table 4. Different Operating Conditions**

case	O <sub>2</sub> (scfh)	C <sub>3</sub> H <sub>6</sub> (scfh)	air (scfh)	N <sub>2</sub> (scfh)	$\dot{m}$ (kg/s)	$\phi$	$x$
1 (baseline)	578.0	176.0	857.0	28.5	18.10	1.045	3.969
2 (air †33%)	578.0	176.0	1139.8	28.5	20.98	0.969	4.895
3 (air †33%)	578.0	176.0	574.2	28.5	15.22	1.134	2.885
4 (O <sub>2</sub> †33%)	768.7	176.0	857.0	28.5	20.24	0.835	3.171
5 (O <sub>2</sub> †33%)	387.3	176.0	857.0	28.5	15.95	1.396	5.303
6 (C <sub>3</sub> H <sub>6</sub> †33%)	578.0	234.1	857.0	28.5	18.95	1.390	3.969
7 (C <sub>3</sub> H <sub>6</sub> †33%)	578.0	117.9	857.0	28.5	17.24	0.700	3.969
8 (†33%)	768.7	234.1	1139.8	37.9	24.07	1.045	3.969
9 ( $\dot{m}$ †33%)	387.3	117.9	574.2	19.1	12.13	1.045	3.969

have the same value of  $x$  (about 4.0), under which the equivalence ratio associated with the peak temperature is around 1.2 according to our previous discussion. Equilibrium temperature in case 7 is the lowest because

**Table 5. Gas Properties for Different Operating Conditions**

case	$P_{eq}$ (bar)	$T_{eq}$ (K)	$\overline{M}_{pr}$ ( $10^{-3}$ kg/mol)	$T_t$ (K)	$\rho_t$ (kg/m <sup>3</sup> )	$v_t$ (m/s)	$(\rho v^2)_t$ ( $10^5$ kg m <sup>-1</sup> s <sup>-2</sup> )
1 (baseline)	6.79	3128	26.1	2812	0.428	1050	4.72
2 (air 133%)	7.66	3056	26.8	2747	0.509	1023	5.33
3 (air 133%)	5.89	3197	25.0	2874	0.349	1083	4.09
4 (O <sub>2</sub> 133%)	7.47	3112	26.8	2802	0.487	1032	5.19
5 (O <sub>2</sub> 133%)	5.98	3008	25.0	2693	0.376	1054	4.18
6 (C <sub>3</sub> H <sub>6</sub> 133%)	7.34	3128	24.4	2805	0.433	1087	5.11
7 (C <sub>3</sub> H <sub>6</sub> 133%)	6.05	2925	27.9	2630	0.436	982	4.21
8 ( <i>m</i> 133%)	9.06	3159	26.1	2842	0.567	1054	6.30
9 ( <i>m</i> 133%)	4.52	3084	26.0	2772	0.288	1045	3.15

**Table 6. Thermophysical Properties of the Powder Particles**

parameter	value
powder	Ni
density (kg/m <sup>3</sup> )	8900
specific heat (J kg <sup>-1</sup> K <sup>-1</sup> )	471
melting point (K)	1727
latent heat (J/kg)	$3 \times 10^5$
diameter ( $\mu$ m)	1–100

its equivalence ratio is only 0.7. Although the equivalence ratios in cases 2 and 6 are quite different, the temperatures are almost the same. This is because these two equivalence ratios are located on opposite sides of the optimal equivalence ratio and the total mass flow rates differ slightly. The temperatures are quite different in cases 5 and 6 although the equivalence ratios are very close because the mass flow rates are different. Note that a higher mass flow rate favors a higher pressure and, accordingly, a higher equilibrium temperature. Case 3 has the lowest  $x$  and an equivalence ratio close to the optimal one, as a consequence; its equilibrium temperature is the highest, compared to cases 1 and 2, even when the total mass flow rate is low.

On the other hand, the combustion pressure under the above operating conditions is roughly a linear function of the total mass flow rate and changes little with the gas composition. This is because the average molecular weight of the reaction product mixture is  $24\text{--}28 \times 10^{-3}$  kg/mol, and the temperature is  $2.9\text{--}3.1 \times 10^3$  K. Consequently, the sonic velocity does not vary much, and the pressure is proportional to the total mass flow rate (which is in agreement with eq 29).

**4.3. Analysis of Particle Velocity and Temperature.** In the fabrication of nanostructured coatings, it is crucial to maintain a high particle temperature at the point of impact on the substrate and, at the same time, to prevent particles from being superheated, because it is precisely the small grain size that contributes to the superior qualities of nanostructured coatings.<sup>32</sup> It is also of great importance to maintain a high particle velocity at the point of impact on the substrate because the higher the particle velocity, the denser the coating. We simulated the Diamond Jet hybrid HVOF process model under the baseline operating conditions given in Table 4 for nickel (particle properties are given in Table 6), and the results for the in-flight particle velocity, temperature, and melting ratio are shown in Figure 11. Particles of small sizes can reach very high velocities during flight; however, their velocities drop more sharply than those of larger particles because of their smaller momentum inertias. Furthermore, they can be heated to the melting point in a short time and can be fully melted during flight; however, they might eventually be in a coexistence state of liquid and solid

or even in a solid state after a long enough distance. Smaller particles tend to change their temperatures easily because of their smaller thermal inertias. For particles of large sizes, however, the periods for acceleration and heating are both longer, and their velocity (or temperature) profiles become nearly flat as they approach the same velocity (or temperature) as the gas. In addition, large particles might not reach the melting point and be in the solid state during the entire flight. However, particles of medium sizes might become partially melted during flight.

To further understand the behavior of the particles in the HVOF process, we also plotted the velocity, temperature, and melting ratio at the 0.254-m standoff as a function of particle size, as shown in Figure 12. (Note that the configuration of each figure might vary with different spray distances.) Under the baseline operating conditions, particles in the size range of 9–30  $\mu$ m hit the substrate as liquid droplets. Particles of sizes larger than 49  $\mu$ m or less than 5  $\mu$ m are in the solid state at the point of impact on the substrate. Other particles, however, are in a semimolten state when they reach the substrate (where both liquid and solid coexist). It is worth pointing out that, although both very small particles and very large particles hit the substrate in a partially molten state or even in the solid state, their microstructures are not the same because the former have been fully melted during flight.

Figure 13 shows the influences of the particle injection velocity and spray distance on the profiles of the particle velocity, temperature and flight time. It is shown that both disturbances have a minimal effect on the particle velocity. However, their influence on the particle temperature and melting behavior cannot be neglected. This behavior can be explained by the changes in the residence time of the particles in the gas flow field. An increase in the particle injection velocity will result in a decrease in the particle residence time, especially in the high-temperature zone. This is why larger particles are affected to a greater extent. An increase in the spray distance, however, has a greater influence on the temperature of smaller particles. This is because larger particles have greater thermal inertia and do not change their temperature very much after they reach the gas temperature.

**4.4. Modeling of the Powder Size Distribution.** The fact that particle temperature and velocity at the point of impact on the substrate depend strongly on particle size implies that the particle size of the feedstock is one of the key parameters determining coating quality. This property, together with the significant polydispersity of most powders used in the thermal spray process, motivates an attempt to account for the effect of the powder size distribution on the process model, the control problem formulation, and the control-

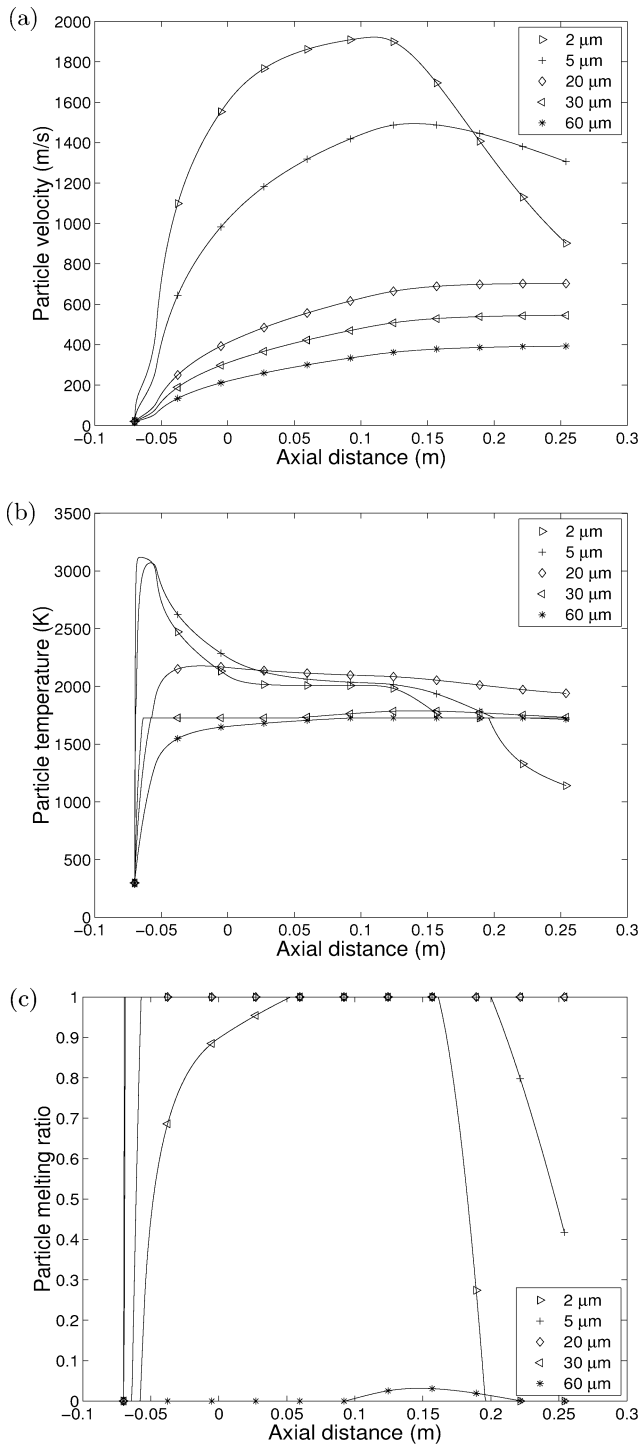


**Figure 11.** Profiles of particle velocity, temperature, and melting ratio along the flow field ( $x = 0$  corresponds to the nozzle exit).

ler design. Previous experimental work<sup>39,40</sup> has shown that log-normal functions can adequately describe the size distribution of many powders used in the HVOF process. To this end, a log-normal function is used in this paper to describe the powder size distribution with the following form<sup>41</sup>

$$f(d_p) = \frac{1}{\sqrt{2\pi}\sigma d_p} \exp\left[-\frac{(\ln d_p - \mu)^2}{2\sigma^2}\right] \quad (32)$$

where  $f(d_p)$  is the size distribution function and  $\mu$  and  $\sigma^2$  are two dimensionless parameters corresponding to

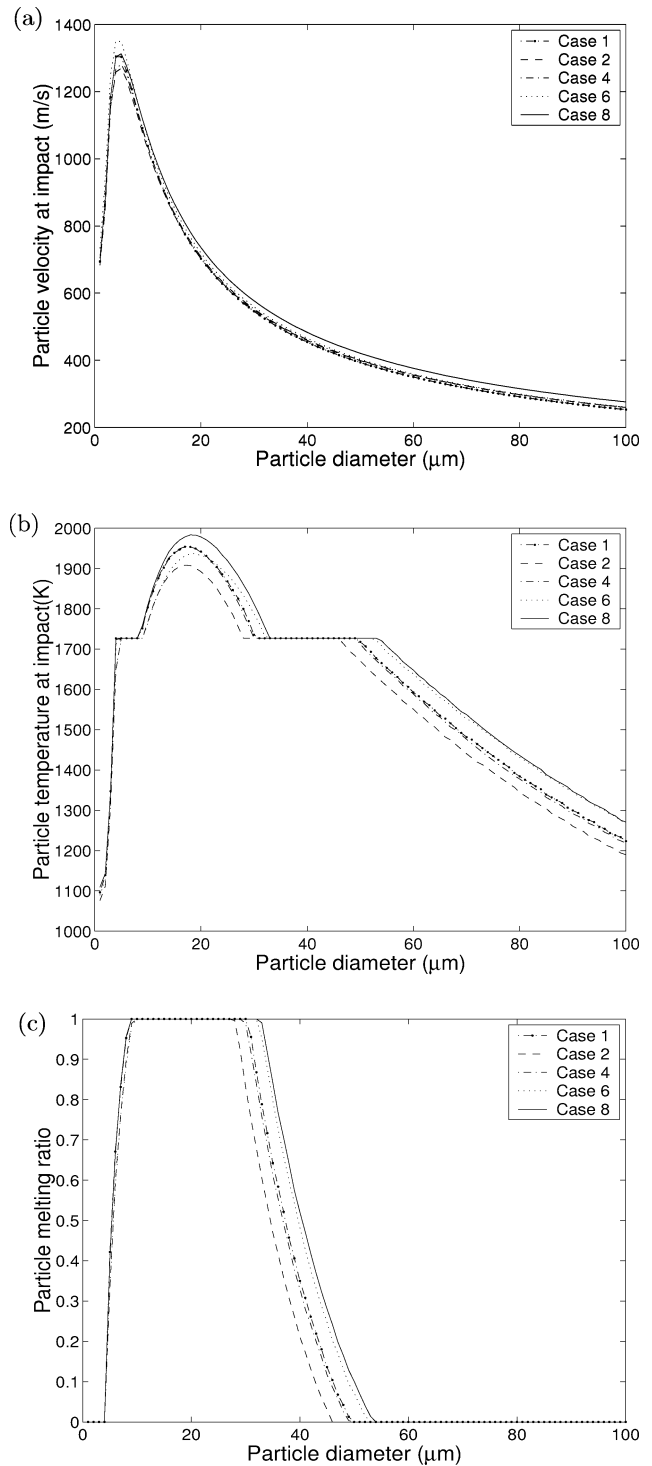


**Figure 12.** Velocity, temperature, and melting ratio at the 0.254-m standoff (point of impact on the substrate) as a function of particle size.

the mean and the variance, respectively, of  $\ln d_p$ , which obeys a normal distribution. For particles that are log-normally distributed,  $\mu$  and  $\sigma$  can be determined using the following formulas<sup>15</sup>

$$\begin{aligned} \mu &= \ln \sqrt[3]{d_{10}d_{50}d_{90}} - 1.831 \left( \ln \sqrt{\frac{d_{90}}{d_{10}}} \right)^2 \\ \sigma &= 0.781 \ln \sqrt{\frac{d_{90}}{d_{10}}} \end{aligned} \quad (33)$$

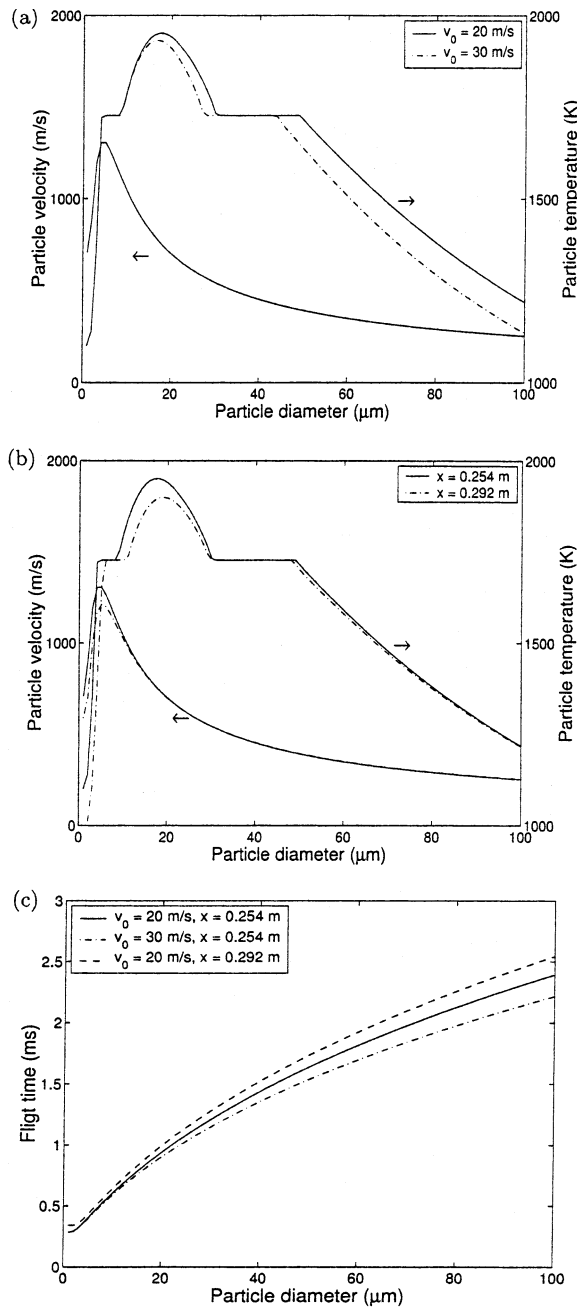


**Figure 13.** Effect of disturbances in the operating conditions (particle injection velocity and spray distance) on the particle velocity, temperature, and flight time.

where  $d_{10}$ ,  $d_{50}$ , and  $d_{90}$  are three characteristic diameters that can be obtained experimentally.<sup>1</sup> Particle coagulation in the HVOF thermal spray process has not been reported in the literature, which can be explained by the following argument. The average distance between individual particles in the HVOF thermal spray process can be estimated from the analysis of Crowe et al.<sup>42</sup> Specifically

$$\frac{L_d}{d_p} = \left( \frac{\pi}{6} \frac{1 + \kappa}{\kappa} \right)^{1/3} \quad (34)$$

where  $L_d$  is the distance between two particles and  $\kappa$  is the ratio of the particle loading to particle/gas density ratio. Usually the particle loading is about 4%, and the density ratio is about  $10^3$ – $10^4$ ; therefore,  $L_d/d_p$  is about

20–50, which implies that the individual powder particles can be considered to be isolated from each other. Therefore, in this work, we assume that particle coagulation is negligible and that the powder size distribution does not change during flight.

There are many ways to define average powder properties. For example, they can be averaged with respect to particle number or particle volume. In this work, the average powder properties (PP) are calculated on the basis of the particle volume because larger particles have a stronger influence on the coating properties than smaller ones. Volume-based average powder properties can be computed as follows:

$$\overline{PP} = \frac{\int_0^\infty \frac{1}{6} \pi d_p^3 PP(d_p) f(d_p) d(d_p)}{\int_0^\infty \frac{1}{6} \pi d_p^3 f(d_p) d(d_p)} \quad (35)$$

## 5. Feedback Control of the HVOF Thermal Spray Process

**5.1. Control Problem Formulation and Controller Design.** On the basis of model predictions and available experimental observations, the control problem for the HVOF process is formulated as the one of regulating the volume-based averages of the melting ratio and particle velocity at the point of impact on the substrate (these are the variables that directly influence the coating microstructure and porosity; see the modeling and analysis discussion in the second paper of this series<sup>19</sup>) by manipulating the flow rates of propylene, oxygen, and air at the entrance of the HVOF thermal spray gun. From the analysis in the previous sections, it follows that the gas momentum flux, which is approximately proportional to the drag force, and the gas temperature, whose difference from the particle temperature provides the driving force for particle heating, can be almost independently adjusted by manipulating the combustion pressure and the equivalence ratio. To develop a feedback controller that can be readily implemented in practice, the manipulation of the combustion pressure and equivalence ratio is realized by adjusting the flow rates of propylene,  $u_1(t)$ ; oxygen,  $u_2(t)$ ; and air,  $u_3(t)$ . Because of the almost decoupled nature of the manipulated input/controlled output pairs, two proportional integral (PI) controllers are used to regulate the process. Specifically, the controllers have the form

$$\dot{\zeta}_i = y_{sp_i} - y_i, \quad \zeta_i(0) = 0, \quad i = 1, 2$$

$$u_i = K_{c_i} \left[ (y_{sp_i} - y_i) + \frac{1}{\tau_{c_i}} \zeta_i \right] + u_{0_i}, \quad i = 1, 2 \quad (36)$$

$$\{u_1, u_2, u_3\} = f(u'_1, u'_2, x)$$

where  $y_{sp_i}$  is the desired set-point value and  $y_i$  is the value of the output obtained from the measurement system ( $y_1$  is the volume-based average of the particle velocity and  $y_2$  is the volume-based average of the particle melting ratio).  $u'_1$  is the combustion pressure, and  $u'_2$  is the equivalence ratio.  $K_{c_i}$  is the proportional gain, and  $\tau_{c_i}$  is the integral time constant of the  $i$ th controller. The third equation makes use of the process model. To keep the problem simple, the ratio of air to oxygen (or  $x$ ) is fixed. We note that the relationship between the gas temperature and the equivalence ratio is not monotonic. Above the optimal equivalence ratio

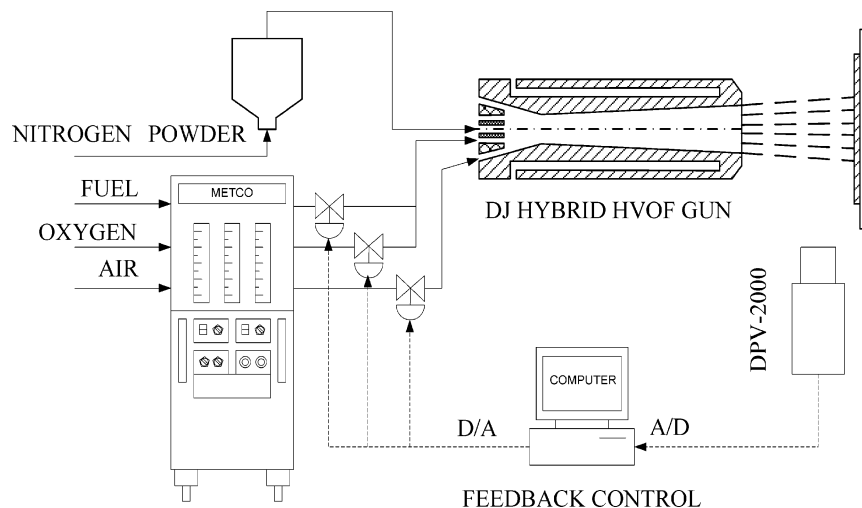


**Figure 14.** Schematic of the proposed feedback control system.

(about 1.2 for  $x = 3.97$ ), the gas temperature decreases as the equivalence ratio increases. Therefore,  $K_{c2}$  and  $\tau_{c2}$  should be replaced by  $-K_{c2}$  and  $-\tau_{c2}$  when the equivalence ratio is above the optimum value. The design of a model-based feedback control system employing nonlinear control techniques for particulate processes,<sup>43–49</sup> as well as applications of the control system to an experimental system, will be the subject of future work.

Regarding the practical implementation of the proposed control system (see Figure 14 for a schematic) on the Diamond Jet hybrid HVOF thermal spray, we note that the chamber pressure and the equivalence ratio can be readily manipulated in real time by adjusting the mass flow rates of fuel, oxygen, and air. The velocities and temperatures of individual particles can be measured experimentally using nonintrusive optical techniques, such as laser doppler velocimetry,<sup>50</sup> particle imaging velocimetry,<sup>51,52</sup> and two color pyrometry.<sup>53–55</sup> However, it is not possible to directly measure the degree of melting of individual particles and consequently, the average degree of melting of the entire particle size distribution. To overcome this limitation, one needs to use an estimation scheme based on modeling equations that describe the evolution of the particle temperature, velocity and degree of particle melting coupled with the available gas-phase measurements to estimate average particle melting ratio at the point of impact on the substrate. The estimates obtained by this model can be further improved through comparison with the particle temperature measurements at various locations across the free jet. In the simulation section (section 5.2, below), we include the results of a closed-loop simulation in the presence of measurement errors to evaluate the effect of such errors on closed-loop performance; the detailed development of an estimation scheme for the particle melting ratio is the subject of future work. The controller then obtains information from the measurement system, and makes decisions, which are sent to the controlled valves (total flow of gases to the process and oxygen/fuel ratio), to adjust the manipulated input variables until the deviation of the controlled outputs from their corresponding set-point values falls within a given tolerance. One of the great advantages of feedback control is that it can compensate for the effect of disturbances in the process operating conditions.

**Table 7. Process and Controller Parameters Used in the Closed-Loop Simulation**

parameter	value
$K_{c1}$	$5 \times 10^{-3}$
$K_{c2}$	0.1
$\tau_1$	$5 \times 10^{-2}$
$\tau_2$	$5 \times 10^{-2}$
$d_{10}$ ( $\mu\text{m}$ ) <sup>a</sup>	15
$d_{50}$ ( $\mu\text{m}$ )	35
$d_{90}$ ( $\mu\text{m}$ )	77
$\phi$	1.0

<sup>a</sup> Powders are assumed to be log-normally distributed, and  $d_{10}$ ,  $d_{50}$ , and  $d_{90}$  are three characteristic diameters whose corresponding cumulative weight function values are 0.1, 0.5, and 0.9, respectively.

**5.2. Simulation Results of the HVOF Process Model under Feedback Control.** In this subsection, simulation runs of the closed-loop system are presented. The outputs  $y_1(t)$  and  $y_2(t)$  are computed by averaging the individual particle velocity and melting ratio data obtained from the process model. To account for the powder size distribution, we first fit a log-normal distribution and calculate the size range to capture more than 99 wt % of the particles. We then divide this size range into 100 intervals to perform the integration. (Further increasing the number of discretization intervals did not change the accuracy of the computed results.)<sup>15,16</sup> This requires that 400 ordinary differential equations be solved simultaneously for each process simulation. The parameters used in the closed-loop system simulations are listed in Table 7.

Several simulation runs of the process model under the feedback controller were performed to evaluate the ability of the controller to (a) drive the melting ratios and velocities of the particles at the point of impact on the substrate to desired set-point values, (b) attenuate the effects of disturbances on process operating conditions, and (c) compensate for the effects of measurement errors. The first simulation studies the behavior of the closed-loop system in the presence of changes in the set point. Initially, the process is assumed to operate at the baseline conditions, and at time  $t = 10$  s, the average particle velocity set-point value increases by 5%, and the average particle melting ratio set-point value decreases by 5%. Figure 15 shows how the controlled outputs and manipulated inputs, as well as the total mass flow rate and the equivalence ratio, respond in the case of requesting such changes in the set-point

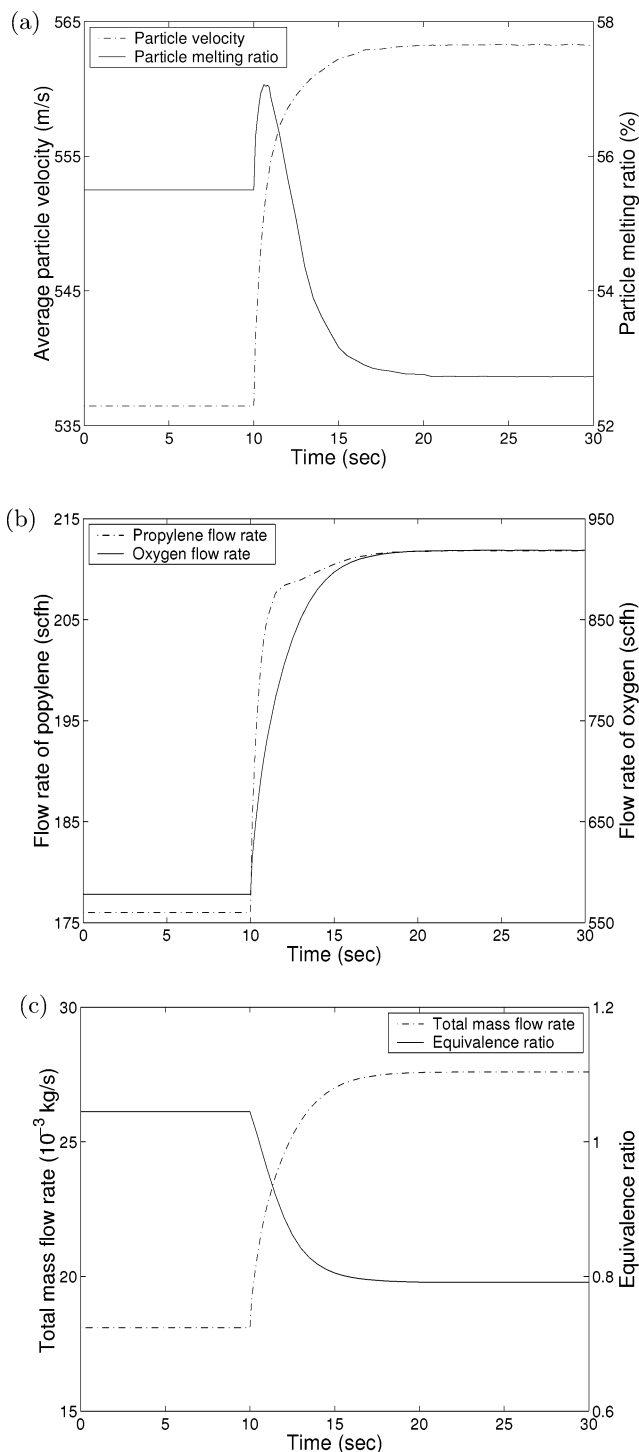


**Figure 15.** Profiles of controlled outputs (average particle velocity and melting ratio), manipulated inputs (flow rates of propylene, oxygen, and air), and total mass flow rate and equivalence ratio under the request of a 5% increase in the average particle velocity and a 5% decrease in the melting ratio. The control problem formulation accounts for the effect of the powder size distribution.

values. The feedback controller drives the controlled outputs to the new set-points in about 10 s. (Note that 10 s is the time needed for the controlled outputs to reach the new set-point values, not the time for the particles to hit the substrate, which is on the order of  $10^{-3}$  s.) In a typical HVOF process, the powder feed rate is in the range 20–80 g/min, and the thickness of a coating is about 100–300  $\mu\text{m}$ .<sup>31</sup> The deposition efficiency of the HVOF process is around 70%.<sup>56</sup> Considering the

deposition of a coating on a 0.5 m  $\times$  0.5 m substrate, the deposition time can be estimated as

$$t = \frac{200 \times 10^{-6} \text{ m} \times 0.5 \text{ m} \times 0.5 \text{ m} \times 8900 \text{ kg/m}^3}{50 \times 10^{-3} \text{ kg/min} \times 0.7} = 12.7 \text{ min} \quad (37)$$

For a coating with a larger area, the deposition time is even longer, which indicates that the controller is quite effective (compared with the typical time needed for a full coating) and validates the feasibility of the implementation of feedback control on the HVOF process. Note that, in the first 0.8 s, the liquid ratio increases when the equivalence ratio decreases. This is because, in this time period, the mass flow rate and the pressure increase by 22 and 21%, respectively, while the equivalence ratio decreases by 6%. As a result, the increase in gas temperature resulting from the increased pressure outweighs the decrease in temperature resulting from the lower equivalence ratio.

To demonstrate that the proposed formulation of the control problem, which explicitly accounts for the effect of the powder size distribution, leads to a solution of the control problem that is superior (with respect to the control action needed to achieve the desired control objectives) to a solution that assumes a monodisperse powder size distribution, the two PI controllers were also implemented on the process model using the same controlled outputs but assuming that the velocity and temperature measurements are based on a single particle whose size is taken to be  $d_p = 35 \mu\text{m}$ , which is equal to the  $d_{50}$  value of the powder size distribution used in our simulation. The corresponding controlled and manipulated variables are displayed in Figure 16. The results show that the desired objectives of 5% changes in the set-point values are not achieved (cf. the controlled output profiles of Figure 15, where the desired set-point change is achieved); this occurs because, as has been previously shown,<sup>16</sup> the behavior of an individual particle is insufficient to represent the behavior of the entire powder size distribution. This makes clear the need to account for the effect of the powder size distribution in the control problem formulation and solution.

To test the robustness of the proposed control problem formulation and of the feedback controller, the problem of controlling the HVOF process in the presence of disturbances was studied. Figures 17 and 18 show the controlled output and manipulated input profiles in the presence of a disturbance (20% increase and 20% decrease, respectively) in the spray distance occurring at  $t = 10$  s. Without control, the process jumps to a new steady state in a very short time (owing to the very short time of particle flight); the particle velocity in each case drops instantaneously. The reason for this result is that the particles are usually accelerated first and then decelerated in the external field, so that there is an optimal spray distance. Nevertheless, the disturbances in the spray distance do not have a significant effect on the particle velocity because the velocity profile of the particles is almost flat as they reach the gas velocity. However, the melting ratio of the particles at the point of impact on the substrate decreases in the former case and increases in the latter case, which can be explained by the change in residence time of the particles in the gas flame. Such variations in the molten state of the particle can have a detrimental effect on the coating

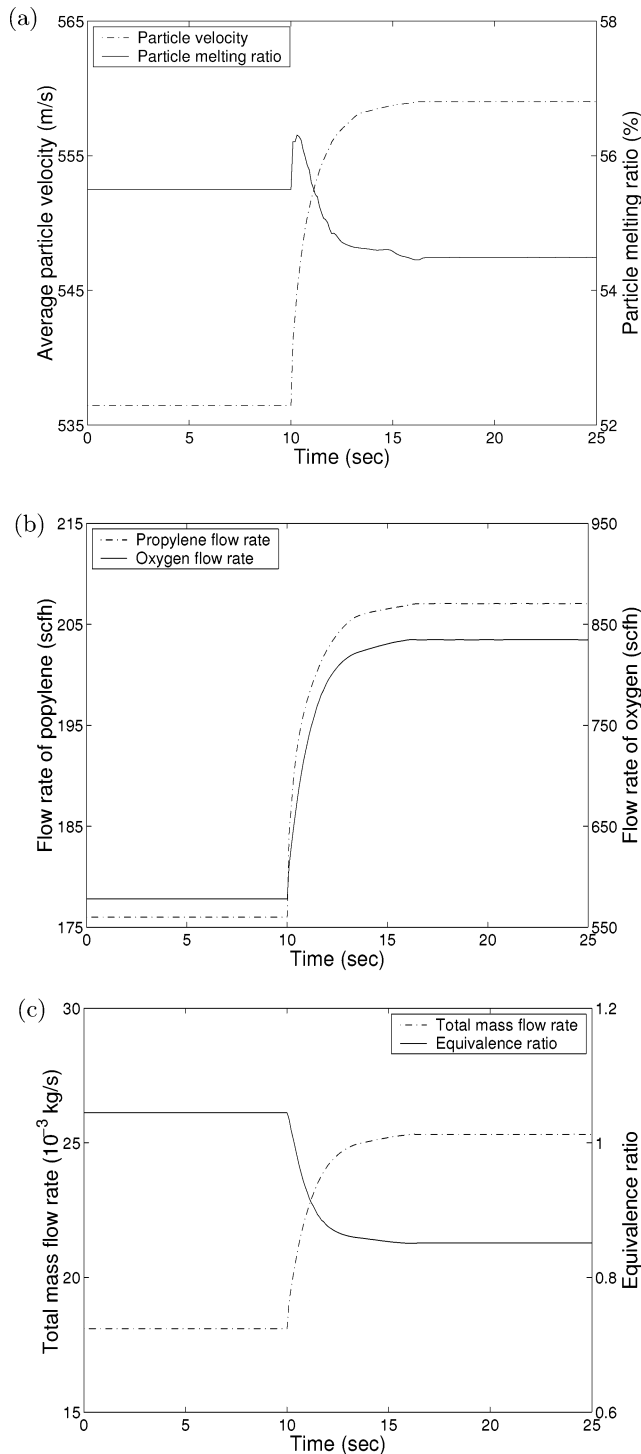


**Figure 16.** Profiles of controlled outputs (average particle velocity and melting ratio), manipulated inputs (flow rates of propylene, oxygen, and air), and total mass flow rate and equivalence ratio under the request of a 5% increase in the average particle velocity and a 5% decrease in the melting ratio. The control problem formulation does not account for the effect of the powder size distribution.

microstructure evolution. Under feedback control, the manipulated inputs drive the process outputs to their original steady-state values in 10–25 s. It is also interesting to see how the controller responds to compensate for this velocity decrease. Whereas it is intuitively expected that the mass flow rate increases in the latter case to increase the particle velocity, the total mass flow rate in the former case decreases to drive the

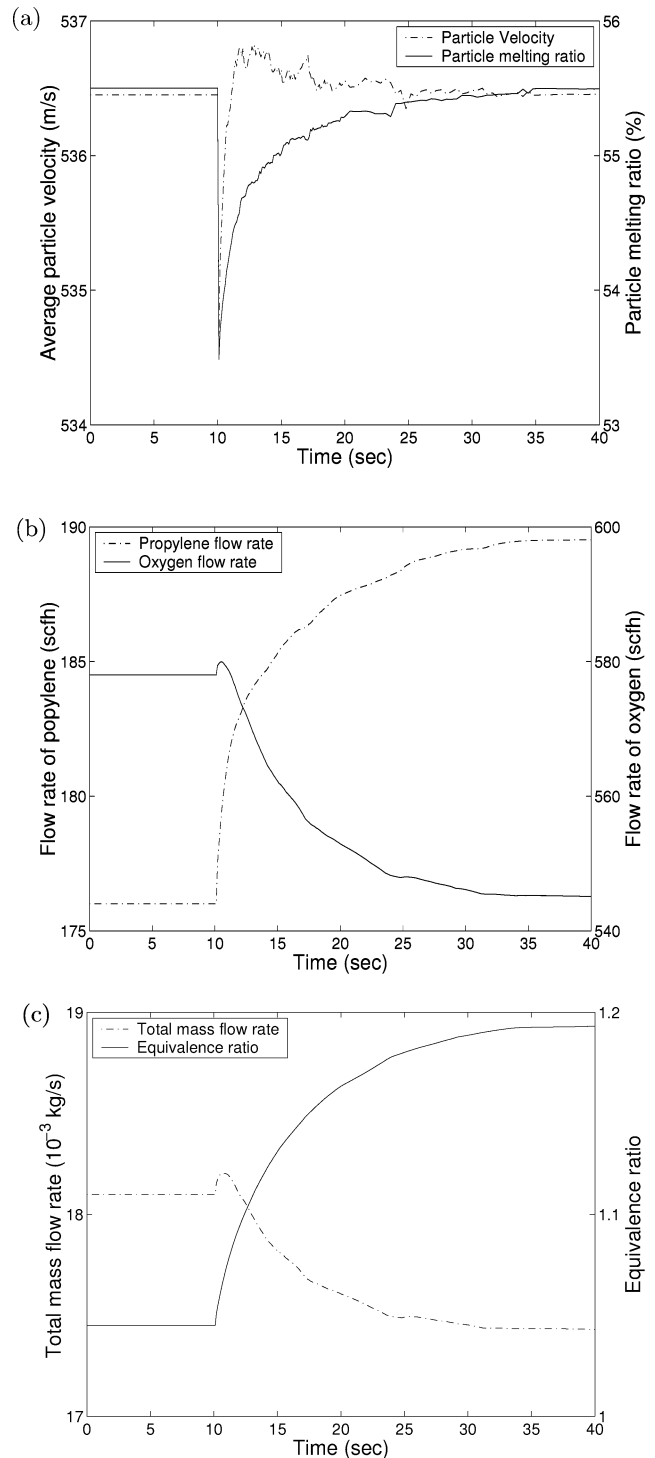


**Figure 17.** Profiles of controlled outputs (average particle velocity and melting ratio), manipulated inputs (flow rates of propylene, oxygen, and air), and total mass flow rate and equivalence ratio in the presence of a disturbance (20% increase) in the spray distance.

particle velocity to its original value. This is because the equivalence ratio continuously increases and the pressure increases even as the total mass flow rate decreases.

Figures 19 and 20 show the controlled output and manipulated input profiles in the presence of disturbances (10% increase and 20% decrease, respectively) in the initial particle velocity at  $t = 10$  s. Without control, the system jumps to a new steady state in a

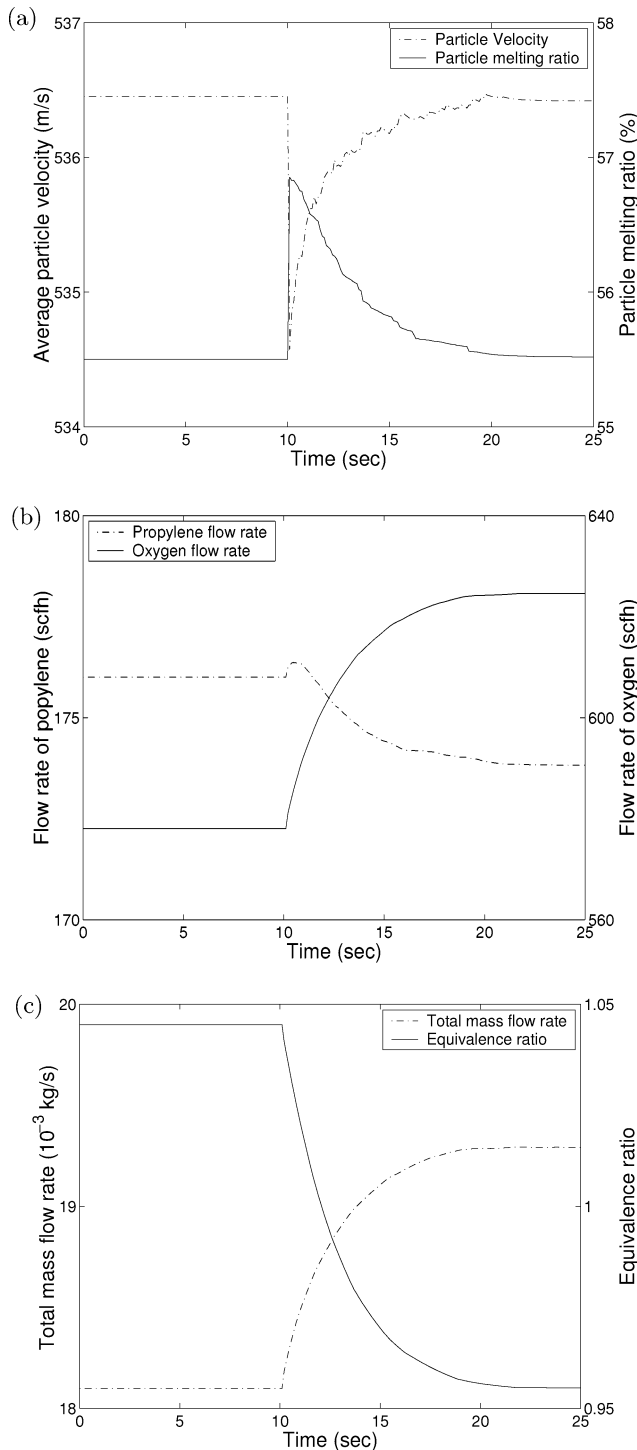


**Figure 18.** Profiles of controlled outputs (average particle velocity and melting ratio), manipulated inputs (flow rates of propylene, oxygen, and air), and total mass flow rate and equivalence ratio in the presence of a disturbance (20% decrease) in the spray distance.

very short time. Whereas the particle velocity changes little in both cases, the particle melting behavior varies a lot. The changes in the particle temperature in both cases can be explained by the residence time of the particles in the flame gas, which is caused by the variation in the particle velocity along the flight, although the particle velocity at the point of impact remains nearly the same. Under feedback control, the manipulated inputs drive the process outputs to their original steady-state values in about 20 s.

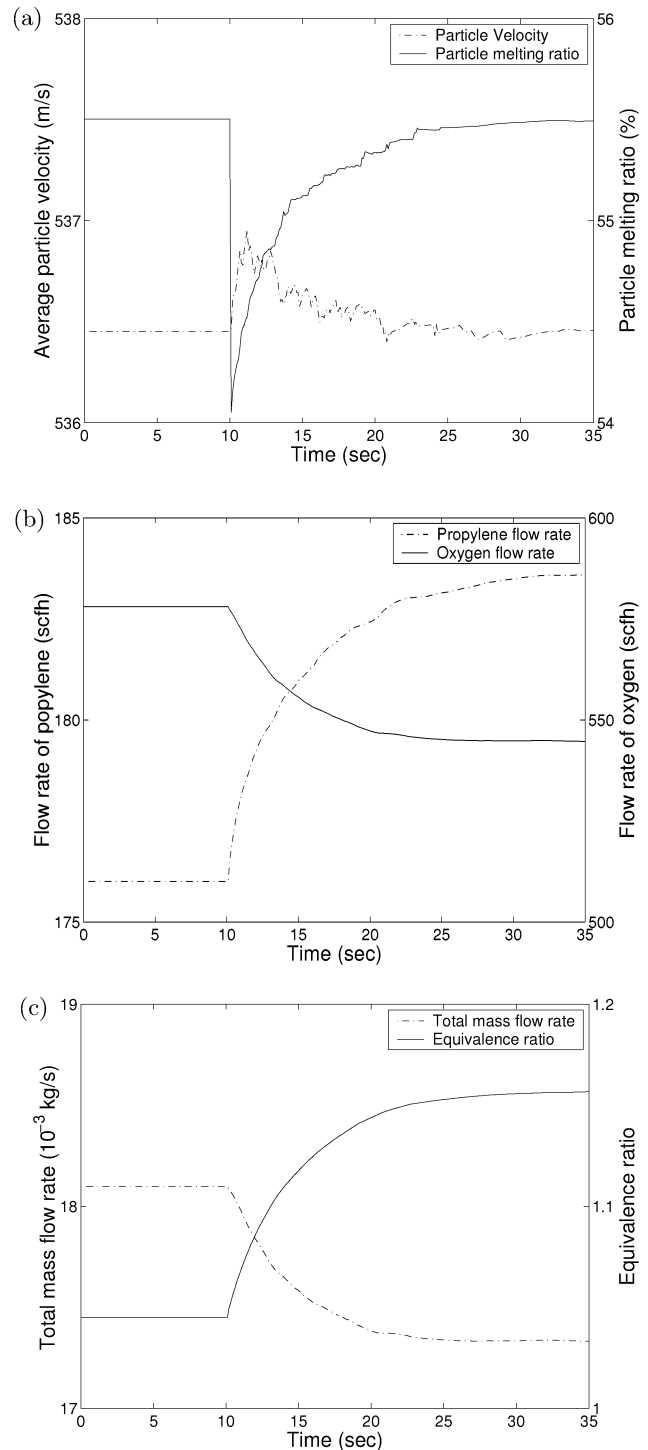


**Figure 19.** Profiles of controlled outputs (average particle velocity and melting ratio), manipulated inputs (flow rates of propylene, oxygen, and air), and total mass flow rate and equivalence ratio in the presence of a disturbance (10% increase) in the particle injection velocity.

Another source of disturbance to the process operation, especially in an industrial environment, is the variation in the size distribution of the powder during the operation of the HVOF process. According to the analysis of the previous sections, this might have a significant influence on the particle velocity and particle temperature at the point of impact on the substrate. In the following simulation, it is assumed that the process is at steady state in the first 100 s and then the powder size distribution changes gradually. (Specif-

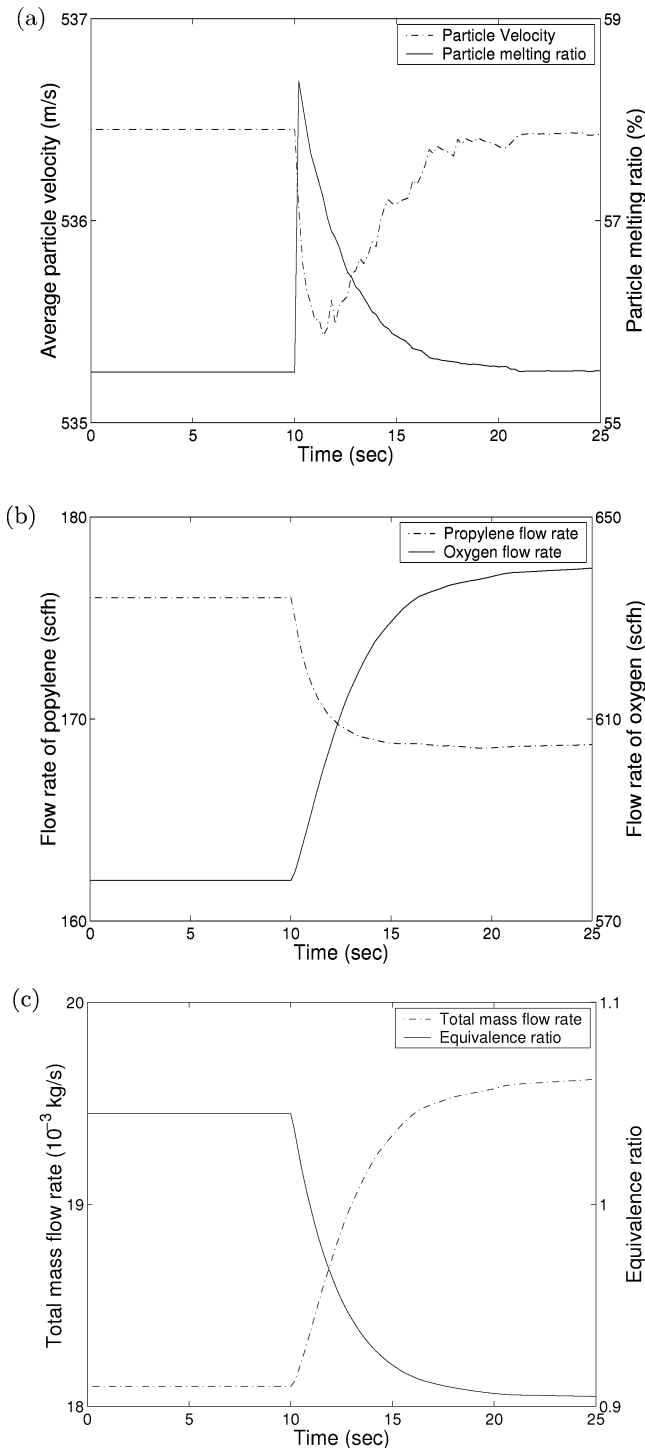


**Figure 20.** Profiles of controlled outputs (average particle velocity and melting ratio), manipulated inputs (flow rates of propylene, oxygen, and air), and total mass flow rate and equivalence ratio in the presence of a disturbance (20% decrease) in the particle injection velocity.

ically, in the following calculation,  $\mu$  increases according to the expression  $\mu = \mu_0[1 + 0.03(1 - e^{-t/100})]$ , and  $\sigma^2$  is kept constant.) Figure 21 shows the controlled outputs and the manipulated inputs, as well as the total mass flow rate and the equivalence ratio, in the presence of such a variation in the powder size distribution. Under feedback control, both the particle velocity and melting ratio fluctuate in a very narrow range around the desired set-point values. We note that  $\varphi$  changes rather sharply compared to the change in  $\dot{m}_{\text{Fuel}}$  and  $\dot{m}_{\text{O}_2}$

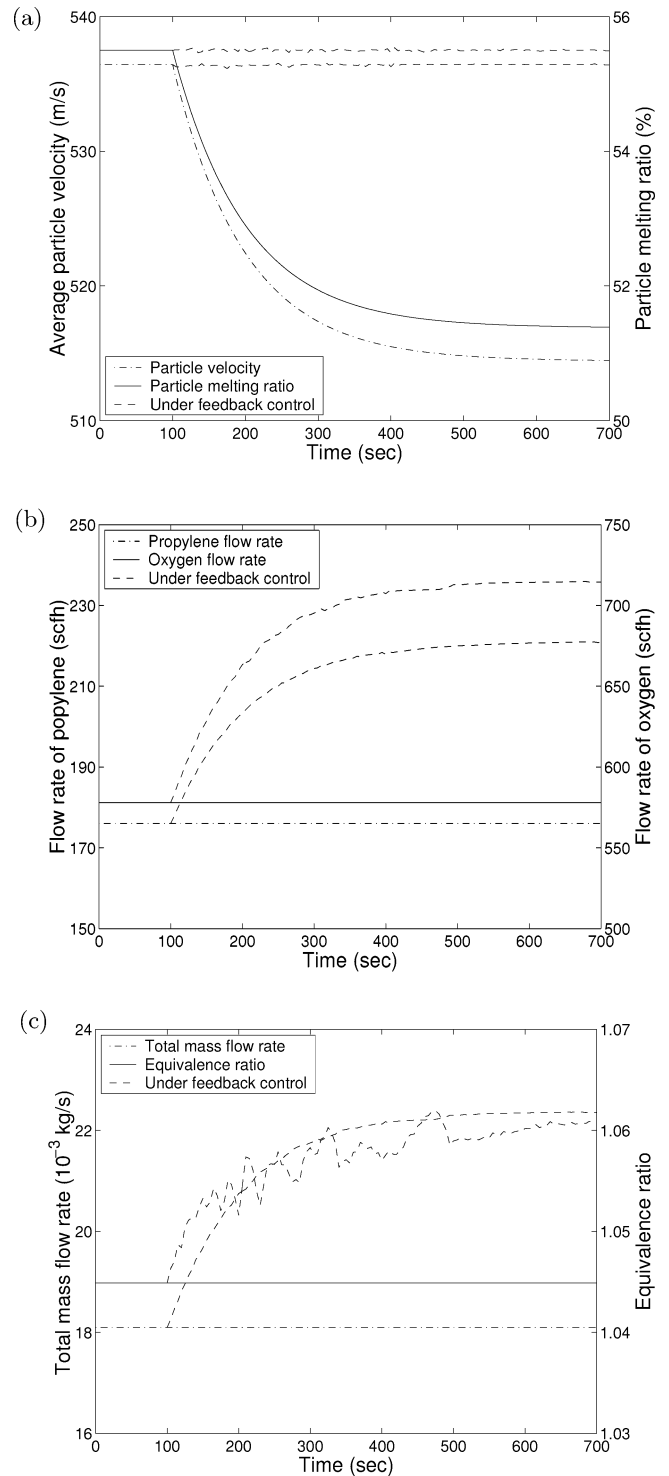


**Figure 21.** Profiles of controlled outputs (average particle velocity and melting ratio), manipulated inputs (flow rates of propylene, oxygen, and air), and total mass flow rate and equivalence ratio in the presence of variations in the powder size distribution.

because both  $\dot{m}_{\text{Fuel}}$  and  $\dot{m}_{\text{O}_2}$  have an influence on  $\varphi$  ( $\varphi = \dot{m}_{\text{Fuel}}/\dot{m}_{\text{O}_2} \times 4.5$ ). For example,  $\varphi$  will go up sharply if  $\dot{m}_{\text{Fuel}}$  increases while  $\dot{m}_{\text{O}_2}$  decreases and go down sharply in the opposite case. When no control is used, in which case the flow rate of each stream is kept constant, both the velocity and melting ratio of the particles decrease with time, which might have an undesirable effect on the resulting coating properties.

To demonstrate that the proposed formulation of the control problem is robust with respect to measurement

errors, we implemented the developed control system on the process model under the request of a 5% increase in the average particle melting ratio set-point value and a 5% decrease in the average particle velocity set-point value at time  $t = 10$  s, assuming that there are errors in the values of the average velocity and degree of melting used in the controller. In the closed-loop simulation, we assume that the estimation errors follow an exponentially decaying function with an initial error of 10%. The corresponding controlled and manipulated variables are shown in Figure 22. The results show that the desired control objective of a 5% change in the set-point values is eventually achieved (cf. the controlled output profiles of Figures 15 and 22); this demonstrates that the proposed formulation of the control problem is robust with respect to measurement errors.

## 6. Conclusions

This article presents a fundamental model and a feedback control system for an industrial high-velocity oxygen-fuel (HVOF) thermal spray process (Diamond Jet hybrid gun, Sulzer Metco, Westbury, NY). The process model describes the evolution of the gas thermal and velocity fields and the motion and temperature of agglomerate particles of different sizes and explicitly accounts for the effect of the powder size distribution. In addition to providing useful insight into the in-flight behavior of different-size particles, the model was used to make a comprehensive parametric analysis of the HVOF process. This analysis allowed for the systematic characterization of the influence of controllable process variables such as the combustion pressure and oxygen/fuel ratio, as well as the effect of the powder size distribution, on the values of the particle velocity and temperature at the point of impact on the substrate. Specifically, the study shows that the particle velocity is primarily influenced by the combustion pressure and that the particle temperature is strongly dependent on the fuel/oxygen ratio. These findings are consistent with existing experimental studies and set the basis for the formulation of the control problem for this HVOF process. To develop a feedback controller that can be readily implemented in practice, the control problem was formulated as one of regulating volume-based averages of the melting ratio and velocity of the particles at the point of impact on the substrate (these are the variables that directly influence the coating microstructure and porosity, which, in turn, determine the coating strength and hardness) by directly manipulating the flow rates of fuel, oxygen, and air at the entrance of the HVOF gun. A feedback control system was developed and applied to the process model. Closed-loop simulations demonstrated that the particle velocity and melting ratio at the point of impact on the substrate reached the desired set-point values in a short time, which validates the feasibility of real-time implementation of feedback control on the HVOF thermal spray system. It was also shown that the proposed control problem formulation and feedback control system are robust with respect to disturbances in the spray distance and particle injection velocity, as well as variations in powder size distribution.

In the second article of this series,<sup>19</sup> we present a stochastic model that uses information about the particle velocity, temperature, and degree of melting at the point of impact on the substrate from the model

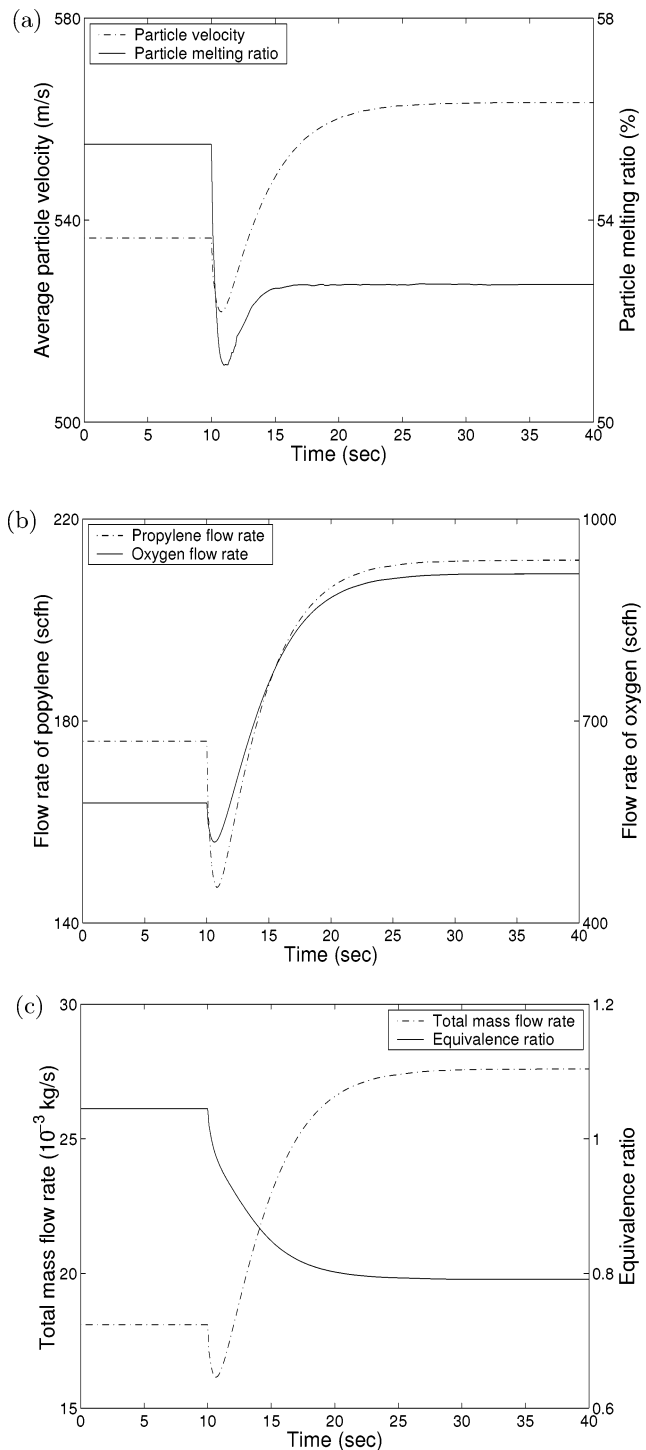


**Figure 22.** Profiles of controlled outputs (average particle velocity and melting ratio), manipulated inputs (flow rates of propylene, oxygen, and air), and total mass flow rate and equivalence ratio under the request of a 5% increase in average particle velocity and a 5% decrease in the melting ratio. Closed-loop simulation in the presence of measurement error.

developed in the present paper to predict the coating porosity and microstructure.

## Acknowledgment

Financial support from a 2001 Office of Naval Research Young Investigator Award, program manager Dr. Lawrence Kabacoff is gratefully acknowledged.

**Notation**

$a$  = sonic velocity (m/s)  
 $a_1$ – $a_9$  = coefficients of the polynomial expression for heat capacity  
 $a_{ij}$  = number of element  $j$  in species  $i$   
 $A$  = cross-sectional area perpendicular to the flow direction ( $m^2$ )  
 $A_p$  = projected area of a particle on the plane perpendicular to the flow ( $m^2$ )  
 $A'_p$  = surface area of the particles ( $m^2$ )  
 $b_1$ – $b_4$  = coefficients of the polynomial expression for viscosity  
 $b_j$  = total number of elements  $j$  in each molecule of reactants (mol/kg)  
 $Bi$  = Biot number  
 $c_1$ – $c_4$  = coefficients of the polynomial expression for thermal conductivity  
 $c_p$  = heat capacity at constant pressure ( $J\ mol^{-1}\ K^{-1}$  for gas or  $J\ kg^{-1}\ K^{-1}$  for particle)  
 $C_D$  = drag coefficient  
 $d$  = particle diameter (m)  
 $D$  = diameter of the gun barrel (m)  
 $E$  = kinetic energy (J)  
 $f_p$  = liquid fraction or melting degree of the particles  
 $F$  = cumulative volume or weight function  
 $G$  = Gibbs energy (J/kg)  
 $h$  = heat-transfer coefficient ( $W\ m^{-2}\ K^{-1}$ )  
 $H$  = enthalpy (J/mol)  
 $K_c$  = proportional gain  
 $K_1, K_2$  = factors used in eq17  
 $l$  = total number of chemical elements involved in the system  
 $L_d$  = average distance between particles (m)  
 $L_{pc}$  = potential core length of the supersonic free jet (m)  
 $m$  = mass (kg)  
 $M$  = molecular weight (kg/mol)  
 $\mathcal{M}$  = Mach number  
 $Nu$  = Nusselt number  
 $P$  = pressure (Pa)  
 $PP$  = particle properties  
 $Pr$  = Prandtl number  
 $R$  = gas constant ( $8.314\ J\ mol^{-1}\ K^{-1}$ )  
 $Re$  = Reynolds number  
 $T$  = temperature (K)  
 $t$  = time (s)  
 $u$  = manipulated input  
 $v$  = velocity (m/s)  
 $x$  = coefficient of air in the reaction formula  
 $x_p$  = axial distance (m)  
 $y$  = controlled output  
**Greek Letters**  
 $\alpha, \beta$  = factors used in eqs 13 and 14  
 $\varphi$  = equivalence ratio  
 $\xi$  = stoichiometric coefficient (mol/kg)  
 $\zeta$  = error  
 $\mu_i$  = chemical potential of species  $i$  (J/mol)  
 $\mu$  = mean of Gaussian distribution  
 $\gamma$  = adiabatic constant, ratio of the heat capacity at constant pressure to the heat capacity at constant volume  
 $\rho$  = density ( $kg/m^3$ )  
 $\phi$  = sphericity, defined as the ratio of the surface area of a sphere with equivalent volume to the actual surface area of a particle  
 $\eta$  = viscosity ( $Pa\cdot s$ )  
 $\tau_c$  = integral time constant  
 $\tau_p$  = characteristic time for particle motion (s)  
 $\kappa$  = ratio of the particle loading to particle/gas density ratio  
 $\lambda$  = thermal conductivity ( $J\ m^{-2}\ K^{-1}$ )

$\lambda_i$  = Lagrangian multiplier

$\omega_p$  = characteristic time for particle heating (s)

**Superscripts and Subscripts**

$a$  = atmospheric conditions  
 $b$  = back conditions  
 $bl$  = baseline conditions  
 $e$  = exit conditions  
 $g$  = properties related to the gas  
 $i, j$  = indices  
 $in$  = inlet  
 $l$  = liquid  
 $p$  = properties related to the particles  
 $pr$  = products  
 $re$  = reactants  
 $st$  = stoichiometric conditions  
 $t$  = throat  
 $T$  = total  
 $\emptyset$  = standard conditions  
 $(\bar{\cdot})$  = average

**Literature Cited**

- (1) Lau, M. L.; Jiang, H. G.; Nuchter, W.; Lavernia, E. J. Thermal Spraying of Nanocrystalline Ni Coatings. *Phys. Status Solidi A* **1998**, *166*, 257–268.
- (2) Cheng, D.; Trapaga, G.; McKelliget, J. W.; Lavernia, E. J. Mathematical Modeling of High Velocity Oxygen Fuel Thermal Spraying: An Overview. *Key Eng. Mater.* **2001**, *197*, 1–25.
- (3) Tellkamp, V. L.; Lau, M. L.; Fabel, A.; Lavernia, E. J. Thermal Spraying of Nanocrystalline Inconel 718. *Nanostruct. Mater.* **1997**, *9*, 489–492.
- (4) Power, G. D.; Barber, T. J.; Chiappetta, L. M. Analysis of a High Velocity Oxygen-Fuel (HVOF) Thermal Torch. AIAA Paper No. 92-3598, presented at AIAA/SAE/ASME/ASEE 28th Joint Propulsion Conference and Exhibit, Nashville, TN, July 6–8, 1992.
- (5) Yang, X.; Eidelman, S. Numerical Analysis of a High-velocity Oxygen-fuel Thermal Spray System. *J. Therm. Spray Technol.* **1996**, *5*, 175–184.
- (6) Hassan, B.; Lopez, A. R.; Oberkampf, W. L. Computational Analysis of a Three-Dimensional High-Velocity Oxygen Fuel (HVOF) Thermal Spray Torch. *J. Therm. Spray Technol.* **1998**, *7*, 71–77.
- (7) Wang, G. X.; Prasad, V.; Sampath, S. Rapid Solidification in Thermal Spray Deposition: Microstructure and Modelling. *Sadhana-Acad. Proc. Eng. Sci.* **2001**, *26*, 35–57.
- (8) Mostaghimi, J.; Chandra, S.; Ghafouri-Azar, R.; Dolatabadi, A. Modeling Thermal Spray Coating Processes: A Powerful Tool in Design and Optimization. *Surf. Coat. Technol.* **2003**, *163–164*, 1–11.
- (9) Gourlaouen, V.; Verna, E.; Beaubien, P. Influence of flame parameters on stainless steel coatings properties. In *Thermal Spray: Surface Engineering via Applied Research, Proceedings of the 1st International Thermal Spray Conference*; Berndt, C. C., Ed.; ASM International: Materials Park, OH, 2000; pp 487–493.
- (10) Zagorski, A. V.; Stadelmaier, F. Full-Scale Modelling of a Thermal Spray Process. *Surf. Coat. Technol.* **2001**, *146–147*, 162–167.
- (11) Annavarapu, S.; Apelian, D.; Lawley, A. Spray Casting of Steel Strip: Process Analysis. *Metall. Trans. A* **1990**, *21*, 3237–3256.
- (12) Mathur, P.; Annavarapu, S.; Apelian, D.; Lawley, A. Spray Casting: An Integral Model for Process Understanding and Control. *Mater. Sci. Eng. A* **1991**, *142*, 261–276.
- (13) Fincke, J. R.; Swank, W. D.; Bewley, R. L.; Haggard, D. C.; Gevelber, M.; Wroblewski, D. Diagnostics and Control in the Thermal Spray Process. *Surf. Coat. Technol.* **2001**, *146–147*, 537–543.
- (14) Moreau, C.; Leblanc, L. Optimization and Process Control for High Performance Thermal Spray Coatings. *Key Eng. Mater.* **2001**, *197*, 27–57.
- (15) Li, M.; Christofides, P. D. Modeling and Analysis of HVOF Thermal Spray Process Accounting for Powder Size Distribution. *Chem. Eng. Sci.* **2003**, *58*, 849–857.

- (16) Li, M.; Christofides, P. D. Feedback Control of HVOF Thermal Spray Process Accounting for Powder Size Distribution. *J. Therm. Spray Technol.*, in press.
- (17) Christofides, P. D. Control of Nonlinear Distributed Process Systems: Recent Developments and Challenges. *AIChE J.* **2001**, *47*, 514–518.
- (18) Knotek, O.; Elsing, R. Monte Carlo Simulation of the Lamellar Structure of Thermally Sprayed Coatings. *Surf. Coat. Technol.* **1987**, *32*, 261–271.
- (19) Shi, D.; Li, M.; Christofides, P. D. Diamond Jet Hybrid HVOF Thermal Spray: Rule-Based Modeling of Coating Microstructure. *Ind. Eng. Chem. Res.* **2004**, *43*, 3653–3665.
- (20) Dolatabadi, A.; Mostaghimi, J.; Pershin, V. Effect of a cylindrical shroud on particle conditions in high velocity oxy-fuel spray process. *J. Mater. Process. Technol.* **2003**, *137*, 214–224.
- (21) Power, G. D.; Smith, E. B.; Barber, T. J.; Chiappetta, L. M. *Analysis of a Combustion (HVOF) Spray Deposition Gurr*, UTRC Report 91-8; United Technologies Research Center: East Hartford, CT, 1991.
- (22) Swank, W. D.; Fincke, J. R.; Haggard, D. C.; Irons, G. HVOF Gas Flow Field Characteristics. In *Thermal Spray Industrial Applications, Proceedings of the 7th National Thermal Spray Conference*; Berndt, C. C., Sampath, S., Eds.; ASM International: Materials Park, OH, 1994; pp 313–318.
- (23) Cheng, D.; Xu, Q.; Trapaga, G.; Lavernia, E. J. A Numerical Study of High-Velocity Oxygen Fuel Thermal Spraying Process. Part I: Gas Phase Dynamics. *Metall. Mater. Trans. A* **2001**, *32*, 1609–1620.
- (24) Oberkamp, W. L.; Talpallikar, M. Analysis of a High-Velocity Oxygen-Fuel (HVOF) Thermal Spray Torch Part 1: Numerical Formulation. *J. Therm. Spray Technol.* **1996**, *5*, 53–61.
- (25) Press, W. H.; Teukolsky, S. A.; Vetterling, W. T.; Flannery, B. P. *Numerical Recipes in C: The Art of Scientific Computing*, 2nd ed.; Cambridge University Press: New York, 1997.
- (26) Gordon, S.; McBride, B. J. *Computer Program for Calculation of Complex Chemical Equilibrium Compositions and Applications*, NASA Reference Publication 1311; Lewis Research Center: Cleveland, OH, 1994.
- (27) Roberson, J. A.; Crowe, C. T. *Engineering Fluid Dynamics*, 6th ed.; John Wiley & Sons: New York, 1997.
- (28) Jiang, L. Y.; Sisljan, J. P. Velocity and Density Measurements in Supersonic High-Temperature Exhaust Plumes. *AIAA J.* **1998**, *36*, 1216–1222.
- (29) Cheng, T. S.; Wehrmeyer, J. A.; Pitz, R. W.; Jarrett, O.; Northam, G. B. Raman Measurement of Mixing and Finite-Rate Chemistry in a Supersonic Hydrogen–Air Diffusion Flame. *Combust. Flame* **1994**, *99*, 157–173.
- (30) Tawfik, H. H.; Zimmerman, F. Mathematical Modeling of the Gas and Powder Flow in HVOF Systems. *J. Therm. Spray Technol.* **1997**, *6*, 345–352.
- (31) Pawlowski, L. *The Science and Engineering of Thermal Spray Coatings*; John Wiley & Sons: Chichester, U.K., 1995.
- (32) Cheng, D.; Xu, Q.; Trapaga, G.; Lavernia, E. J. The Effect of Particle Size and Morphology on the In-Flight Behavior of Particles during High-Velocity Oxyfuel Thermal Spraying. *Metall. Mater. Trans. B* **2001**, *32*, 525–535.
- (33) Ganser, G. H. A Rational Approach to Drag Prediction of Spherical and Nonspherical Particles. *Powder Technol.* **1993**, *77*, 143–152.
- (34) Geankoplis, C. J. *Transport Processes and Unit Operations*, 3rd ed.; Prentice Hall: Upper Saddle River, NJ, 1993.
- (35) Bird, R. B.; Stewart, W. E.; Lightfoot, E. N. *Transport Phenomena*; John Wiley & Sons: New York, 1960.
- (36) Crowe, C. T.; Stock, D. E. A Computer Solution for Two-Dimensional Fluid–Particle Flows. *Int. J. Numer. Methods Eng.* **1976**, *10*, 185–196.
- (37) Gu, S.; Eastwick, C. N.; Simmons, K. A.; McCartney, D. G. Computational Fluid Dynamic Modeling of Gas Flow Characteristics in a High-Velocity Oxy-Fuel Thermal Spray System. *J. Therm. Spray Technol.* **2001**, *10*, 461–469.
- (38) Mills, D. Sulzer Metco, Westbury, NY. Personal communication, 2003.
- (39) Lima, R. S.; Kucuk, A.; Berndt, C. C. Integrity of nanostructured partially stabilized zirconia after plasma spray processing. *Mater. Sci. Eng. A* **2001**, *313*, 75–82.
- (40) Lavernia, E. J.; Wu, Y. *Spray Atomization and Deposition*; Wiley: New York, 1996.
- (41) Crow, E. L.; Shimizu, K. *Log–Normal Distributions: Theory and Applications*; Marcel Dekker: New York, 1988.
- (42) Crowe, C. T.; Sommerfeld, M.; Tsuji, Y. *Multiphase Flows with Droplets and Particles*; CRC Press: Boca Raton, FL, 1997.
- (43) Chiu, T.; Christofides, P. D. Nonlinear Control of Particulate Processes. *AIChE J.* **1999**, *45*, 1279–1297.
- (44) Chiu, T.; Christofides, P. D. Robust Control of Particulate Processes Using Uncertain Population Balances. *AIChE J.* **2000**, *46*, 266–280.
- (45) El-Farra, N. H.; Chiu, T.; Christofides, P. D. Analysis and Control of Particulate Processes with Input Constraints. *AIChE J.* **2001**, *47*, 1849–1865.
- (46) Christofides, P. D. *Model-Based Control of Particulate Processes*, Particle Technology Series; Kluwer Academic Publishers: Dordrecht, The Netherlands, 2002.
- (47) Kalani, A.; Christofides, P. D. Nonlinear Control of Spatially-Inhomogeneous Aerosol Processes. *Chem. Eng. Sci.* **1999**, *54*, 2669–2678.
- (48) Kalani, A.; Christofides, P. D. Modeling and Control of a Titania Aerosol Reactor. *Aerosol Sci. Technol.* **2000**, *32*, 369–391.
- (49) Kalani, A.; Christofides, P. D. Simulation, Estimation and Control of Size Distribution in Aerosol Processes with Simultaneous Reaction, Nucleation, Condensation and Coagulation. *Comput. Chem. Eng.* **2002**, *26*, 1153–1169.
- (50) Fincke, J. R.; Swank, W. D.; Jeffrey, C. L. Simultaneous measurement of particle size, velocity and temperature in thermal plasmas. *IEEE Trans. Plasma Sci.* **1990**, *18*, 948–957.
- (51) Knight, R.; Smith, R. W.; Xiao, Z.; Hoffman, T. T. Particle Velocity Measurements in HVOF and APS Systems. In *Proceedings of the 7th National Thermal Spray Conference*, ASM International: Materials Park, OH, 1994; pp 331–336.
- (52) Thomson, I.; Pershin, V.; Mostaghimi, J.; Chandra, S. Experimental Testing of a Curvilinear Gas Shroud Nozzle for Improved Plasma Spraying. *Plasma Chem. Plasma Process.* **2001**, *21*, 65–82.
- (53) Swank, W. D.; Fincke, J. R.; Haggard, D. C. A Particle Temperature Sensor for Monitoring and Control of the Thermal Spray Process. In *Advances in Thermal Spray Science and Technology, Proceedings of the 8th National Thermal Spray Conference*; Berndt, C. C., Sampath, S., Eds.; ASM International: Materials Park, OH, 1995; pp 111–116.
- (54) Hanson, T. C.; Hackett, C. M.; Settles, G. S. Independent Control of HVOF Particle Velocity and Temperature. *J. Therm. Spray Technol.* **2002**, *11*, 75–85.
- (55) Fincke, J. R.; Haggard, D. C.; Swank, W. D. Particle Temperature Measurement in the Thermal Spray Process. *J. Therm. Spray Technol.* **2001**, *10*, 255–266.
- (56) Swank, W. D.; Fincke, J. R.; Haggard, D. C.; Irons, G.; Bullock, R. HVOF Particle Flow Field Characteristics. In *Thermal Spray Industrial Applications, Proceedings of the 7th National Thermal Spray Conference*; Berndt, C. C., Sampath, S., Eds.; ASM International: Materials Park, OH, 1994; pp 319–324.

Received for review July 3, 2003

Revised manuscript received October 9, 2003

Accepted October 10, 2003

IE030559I